

Wavelength-encoded laser particles for massively multiplexed cell tagging

Nicola Martino ^{1,2,7}, Sheldon J. J. Kwok^{1,2,3,7}, Andreas C. Liapis ^{1,2}, Sarah Forward², Hoon Jang⁴, Hwi-Min Kim⁴, Sarah J. Wu⁵, Jiamin Wu ^{2,6}, Paul H. Dannenberg^{1,2,3}, Sun-Joo Jang^{1,2}, Yong-Hee Lee⁴ and Seok-Hyun Yun ^{1,2,3*}

Large-scale single-cell analyses have become increasingly important given the role of cellular heterogeneity in complex biological systems. However, no techniques at present enable optical imaging of uniquely tagged individual cells. Fluorescence-based approaches can distinguish only a small number of distinct cells or cell groups at a time because of spectral crosstalk between conventional fluorophores. Here we investigate large-scale cell tracking using intracellular laser particles as imaging probes that emit coherent laser light with a characteristic wavelength. Made of silica-coated semiconductor microcavities, these laser particles have single-mode emission over a broad range from 1,170 nm to 1,580 nm with sub-nanometre linewidths, enabling massive spectral multiplexing. We explore the stability and biocompatibility of these probes in vitro and their utility for wavelength-multiplexed cell tagging and imaging. We demonstrate real-time tracking of thousands of individual cells in a three-dimensional tumour model over several days, showing different behavioural phenotypes.

The emerging understanding of cellular heterogeneity in biology has necessitated new tools for single-cell analysis. Single-cell sequencing has helped to define cell types with increasingly sophisticated details and revealed the critical role of cellular heterogeneity in cancer, stem cell differentiation and epithelial homeostasis^{1–5}. Despite these advances, a major challenge is the ability to tag and distinguish individual cells and track them over time or over the course of different measurements. Fluorescence-based approaches and in particular genetically encoded fluorescent proteins are ideally suited for labelling clones of cells for lineage tracing. However, their limited multiplexing capacity makes it challenging to track single cells reliably in three-dimensional specimens, often requiring high imaging rates to track moving cells (for example, every few minutes in a tumour invasion assay). Biomolecular techniques using unique DNA barcodes can effectively label an almost unlimited number of cells;^{3,6} they are, however, incompatible with imaging and do not enable retention of spatial information. Furthermore, sequencing to read the DNA barcode is destructive, requiring cell dissociation and lysis, and thus sequencing is limited to endpoint measurements only. These limitations highlight the need for unique tags with optical readout.

Although fluorescence microscopy is widely used for cellular imaging⁷, typical fluorophore linewidths, between 30–100 nm, allow no more than a few spectra to fit into the entire visible spectrum without overlap. Consequently, this technique can normally resolve only a handful of labels, preventing concurrent study of many more cell types and subtypes. It is fundamentally challenging to engineer fluorophores or inorganic emitters to have much narrower emission spectra because of the quantum mechanical and thermodynamic broadening of their electronic energy levels. Raman emission from vibrational transitions is narrower (1–2 nm)

but over a relatively limited tuning range (20 nm)⁸. Multiple fluorescence emitters with dissimilar spectra can be combined^{9–11}, but these approaches relying on intensity-based spectral analysis or nanoscale super-resolution are of limited use for large-scale tracking in optically dense tissues owing to wavelength-dependent absorption and scattering. Unlike molecular engineering, photonic principles harnessing optical resonance and amplification could offer a solution. By placing fluorescent emitters inside an optical cavity with a sufficient quality (Q)-factor, laser emission with extremely narrow, sub-nanometre linewidth can be produced¹². Previous efforts using dye-doped microspheres have shown the proof of concept of this photonic approach^{13,14}, but the large resonator sizes of around 10 μm have prohibited practical applications.

Here we show microlasers with massive multiplexing capability and optimized properties for cell tagging and tracking applications. We name these imaging probes laser particles (LPs). To miniaturize laser sizes, we used semiconductor materials with high refractive index and gain in a microdisk geometry^{15,16}. Microdisk lasers have been extensively investigated for on-chip applications, but we have developed methods to detach them from the substrate, suspend them in solution and coat them with a biocompatible and protective layer (Fig. 1a). These LPs occupy only about 0.1% of a typical cell's volume and generate single narrowband emission peaks (below 0.4 nm), tunable across a wide spectral range of 400 nm. We show their stable performance in cells and present methods of identifying tagged cells using LP-stimulated emission (LASE) microscopy. Finally, we demonstrate massively multiplexed tracking of thousands of individual cancer cells in a three-dimensional tumour spheroid invasion assay. Our work establishes LPs as a new class of luminescent probes that expands optical microscopy for large-scale, comprehensive single-cell analysis.

¹Harvard Medical School, Boston, MA, USA. ²Wellman Center for Photomedicine, Massachusetts General Hospital, Boston, MA, USA. ³Harvard-MIT Health Sciences and Technology, Massachusetts Institute of Technology, Cambridge, MA, USA. ⁴Department of Physics, Korea Advanced Institute of Science and Technology, Daejeon, South Korea. ⁵Department of Mechanical Engineering, Massachusetts Institute of Technology, Cambridge, MA, USA. ⁶Department of Automation, Tsinghua University, Beijing, China. ⁷These authors contributed equally: Nicola Martino and Sheldon J. J. Kwok.

*e-mail: syun@hms.harvard.edu

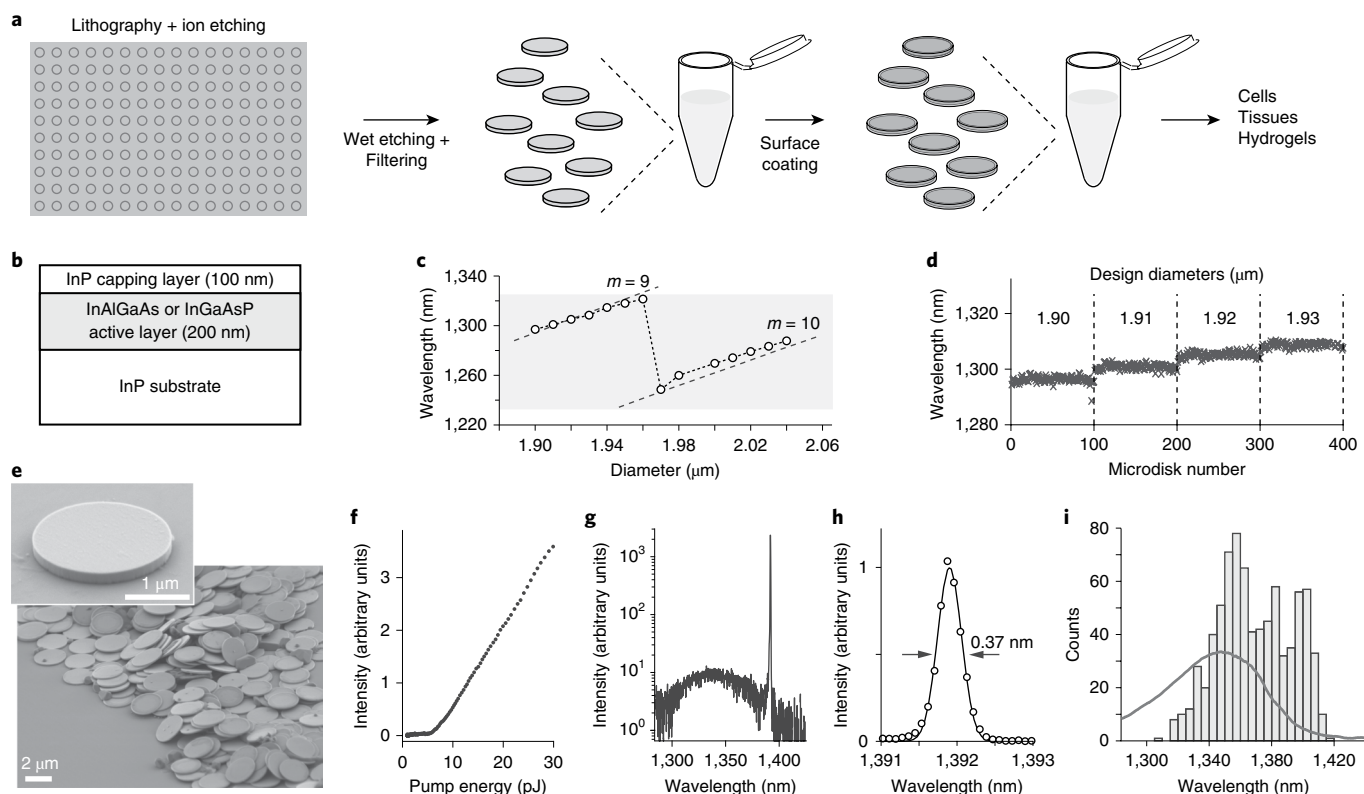


Fig. 1 | Optical properties of semiconductor microdisk lasers. **a**, Schematic of the LP production process. **b**, Structure of the epitaxial wafers used for the fabrication of microdisks. **c**, Lasing wavelength of microdisks (in air) with increasing design diameter varying from 1.9 μm to 2.04 μm in steps of 10 nm. The shaded box corresponds to the gain region of the semiconductor ($\text{In}_{0.73}\text{Ga}_{0.27}\text{As}_{0.58}\text{P}_{0.42}$); dashed lines are the calculated cavity-mode resonances for a microdisk with a refractive index $n = 3.445$. **d**, Lasing wavelength of four groups of microdisks fabricated with different design diameters in 10-nm steps ($N = 100$ per group); standard deviation is around 1 nm. **e**, SEM image of microdisks after detachment. Inset, close-up of a single microdisk. **f**, Output curve of laser emission versus pump energy for a typical cavity. **g**, Typical output emission spectrum of a microdisk above threshold ($E_p = 20$ pJ). **h**, Gaussian fit of the lasing peak. **i**, Histogram of the emission wavelengths of $N = 794$ different microdisks in Matrigel overlaid with the fluorescence of the active material ($\text{In}_{0.53}\text{Al}_{0.13}\text{Ga}_{0.34}\text{As}$).

Single-mode microlasers over a wide spectral range

Of the several semiconductor materials suitable for LPs, we chose the InAlGaAs and InGaAsP quaternary alloys (Fig. 1b), which have small bandgap energy for operation in the second near-infrared window (NIR-II) of 1.0–1.8 μm ¹⁷. This range is attractive owing to its low cell phototoxicity, relatively good penetration into tissues, and no spectral overlap with conventional fluorescent probes^{18,19}. We chose a microdisk design supporting planar whispering gallery mode (WGM) resonances²⁰ because sufficient passive-cavity Q -factors of $>1,000$ can be obtained with micrometre or submicrometre sizes²¹, and the resonance wavelength is tunable by changing its diameter²².

Calculations based on WGM theory (see Supplementary Note 1) predict that, for microdisks with diameters around 2 μm , the sensitivity of the resonance wavelength to small changes in diameter is around 1 nm nm^{-1} . Using electron-beam lithography, we produced batches of microdisks with identical design diameters separated by 10-nm steps. Measurements of their emission wavelengths closely followed theoretical predictions, with a discontinuity when the resonance jumps to a higher order as the diameter increases (Fig. 1c). Measurements of $N = 100$ disks of the same batch show a standard deviation $\sigma = 1$ nm in resonance wavelength (Fig. 1d). Although this spectral uniformity can be useful and may be further improved, in this work we chose to use ultraviolet lithography instead, so that we could produce microdisks in large quantity (about 3.2 million microdisks per square centimetre of wafer) at much faster speed and lower cost than electron-beam lithography. We allowed microdisk

diameters to vary over a range of approximately 200 nm so that the fabricated microdisks have randomly varying wavelengths over the entire gain bandwidth of the semiconductor. We tested different wafer designs including multi-quantum-well structures and bulk semiconductor active layers and obtained comparable performance in terms of laser threshold and emission linewidth (Supplementary Fig. 1). The LPs described below were fabricated from bulk $\text{In}_{0.53}\text{Al}_x\text{Ga}_{0.47-x}\text{As}$ or $\text{In}_x\text{Ga}_{1-x}\text{As}_y\text{P}_{1-y}$ epitaxial layers.

Microdisks were released from the substrate via wet-etching in hydrochloric acid solution and suspended in water after removing debris using size-selective filters. Scanning electron microscopy (SEM) showed reproducible microdisks with smooth edges (Fig. 1e). For optical characterization, the collected microdisks were embedded in three-dimensional hydrogel matrices (Matrigel). Upon optical pumping with a pulsed ytterbium-doped fibre laser, the output emission from each microdisk was analysed using a near-infrared spectrometer. The lasing threshold was observed at a pump energy (E_p) of about 7 pJ for a beam diameter of about 2 μm (Fig. 1f). Above threshold, the output spectrum featured a single peak, with a full-width at half-maximum (FWHM) smaller than 0.4 nm (Fig. 1g, h). The measured intensity varied considerably depending on the microdisk orientation in the hydrogel because WGMs radiate predominantly in the radial direction. The lasing wavelengths of microdisks obtained from a single epitaxial wafer ($\text{In}_{0.53}\text{Al}_{0.13}\text{Ga}_{0.34}\text{As}$ on InP) spanned a broad region across 100 nm, supported by the gain bandwidth of the active medium (Fig. 1i).

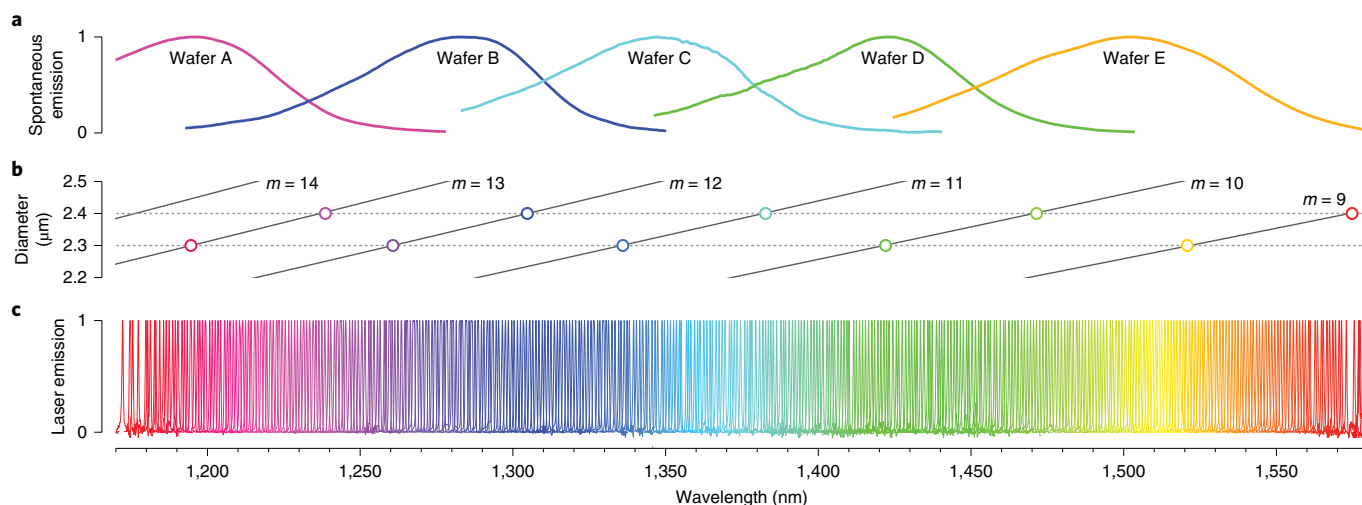


Fig. 2 | Highly multiplexed microdisk lasers. **a**, Normalized fluorescence spectra of the five different semiconductor materials used in this work. Wafer A: $\text{In}_{0.80}\text{Ga}_{0.20}\text{As}_{0.44}\text{P}_{0.56}$; wafer B: $\text{In}_{0.73}\text{Ga}_{0.27}\text{As}_{0.58}\text{P}_{0.42}$; wafer C: $\text{In}_{0.53}\text{Al}_{0.13}\text{Ga}_{0.34}\text{As}$; wafer D: $\text{In}_{0.53}\text{Al}_{0.09}\text{Ga}_{0.38}\text{As}$; and wafer E: $\text{In}_{0.53}\text{Ga}_{0.47}\text{As}_{0.92}\text{P}_{0.08}$. **b**, Calculated resonance wavelengths of WGM modes with mode order m , for different microdisk diameters of 2.2–2.5 μm . Circles represent possible lasing modes obtainable from the five different wafers with microdisk sizes of 2.3 μm and 2.4 μm , respectively. **c**, Normalized laser emission spectra of 400 LPs in a range from 1,170 nm to 1,580 nm with an interval of around 1 nm. All LPs were pumped by a common laser source.

To extend wavelength coverage, we used five semiconductor wafers with their fluorescence peaks separated by about 80 nm (Fig. 2a). We calculated WGM modes²³ as a function of diameter (Supplementary Fig. 2) to confirm that, at a given diameter, only one or two cavity modes fall inside the gain bandwidth of each wafer (Fig. 2b). Experimentally, microdisks of this diameter range generated single-mode laser emission under normal operation conditions. We were thus able to produce batches of microdisks with single-mode emission at different wavelengths across an ultrawide spectral range from 1,170 nm to 1,580 nm (Fig. 2c).

Silica coating of semiconductor microdisks

Unprotected non-oxide semiconductor materials tend to corrode slowly in water and, under photoexcitation, can generate undesirable electrochemical effects^{24,25}. To enable operation in aqueous biological environments, we developed a protocol to passivate the semiconductor surface of the microdisks by coating with silicon dioxide (SiO_2). Each cycle of a modified Stöber process²⁶ produced a silica layer about 50 nm thick, and multiple cycles resulted in thicker coating (Fig. 3a, b). Cross-sectional SEM, energy dispersive X-ray spectroscopy and transmission electron microscopy confirmed uniform silica coating (Fig. 3c, d, Supplementary Fig. 3).

Besides material protection, another critical role of the silica coating is decreasing the evanescent field of cavity modes in the surrounding medium and thereby reducing the sensitivity of lasing wavelengths to changes of external refractive index (n_{ext}). Finite-difference time-domain calculations predict a wavelength dependence on refractive index ($\Delta\lambda/\Delta n_{\text{ext}}$) of 80 nm per refractive index unit (RIU) for uncoated microdisks, which corresponds to a variation of up to 2.4 nm in cell cytoplasm ($n_{\text{ext}} = 1.36\text{--}1.39$)²⁷; however, this sensitivity decreases with increasing coating thickness (Fig. 3e, f). The wavelength sensitivity of 150-nm-coated microdisks deposited on a glass substrate was measured to be 2.9 ± 0.2 nm per RIU, much lower than the 44 ± 1 nm per RIU for uncoated microdisks (Fig. 3g, h).

Stability of LPs in biological environments

Our standard design coating thickness was 100 nm. Coated microdisks embedded in cell-culture hydrogels had a slightly higher threshold pump energy of about 9 pJ than did uncoated lasers in

hydrogels (about 7 pJ), owing to silica having a higher refractive index (1.46) than the hydrogel (1.34) (Fig. 4a). However, silica coating greatly improved the optical stability of microdisks under continuous pulsed excitation ($E_p = 40$ pJ). After one billion pulses, uncoated microdisks in hydrogels showed output power degradation by about 20%, and a decrease in lasing wavelength of 1.5 nm, both of which were worse than in air (Fig. 4b, c and Supplementary Fig. 4). The degradation of uncoated microdisks is attributed to surface oxidation²⁸ and photochemical etching of the semiconductor²⁵. According to our simulations (see Supplementary Note 1), a surface corrosion of the semiconductor by 2 nm causes a spectral blueshift of about 1.8 nm. Silica-coated microdisks in hydrogels were much more stable, producing constant intensity and a minute wavelength shift of 0.1 nm after emitting a billion laser pulses. Hard silica coating greatly reduced the water-induced degradation of semiconductor materials. Over 30 h in cell culture medium, coated samples showed stable lasing wavelengths within 0.4 nm, whereas uncoated semiconductor microdisks degraded with blueshifts of 11 nm (Fig. 4d).

The silica coating also allows LPs to be functionalized using chemistry already developed for silica-coated nanoparticles. For example, incorporation of fluorescent dye into the silica shell allows fluorescence-based detection of LPs, encapsulation of the silica surface with poly(ethylene glycol) can reduce non-specific cellular interactions²⁹, and coating with biotin enables conjugation with biomolecules of interest (Supplementary Fig. 5). Thus, it is possible to conjugate LPs with different chemical species that can provide additional functionalities, such as multimodal imaging, biomolecule sensing, or cell-type-specific targeting^{30–32}.

Biocompatibility of LPs

The silica coating is also essential to improve biocompatibility of the LPs. Several cell lines efficiently internalized LPs within 24 h of incubation in vitro through the non-specific process of macropinocytosis^{32,33} (Fig. 4e and Supplementary Video 1). A live/dead assay showed that whereas coated LPs had no measurable effect on cell viability compared to controls, significant ($P < 0.0001$) toxicity was induced by uncoated microdisks after incubation for 48 and 72 h (Fig. 4f and Supplementary Fig. 6). This result is consistent with previous studies on silica-coated quantum dots, in which the coating layer prevents leakage of toxic ions from the semiconductor surface³⁴.

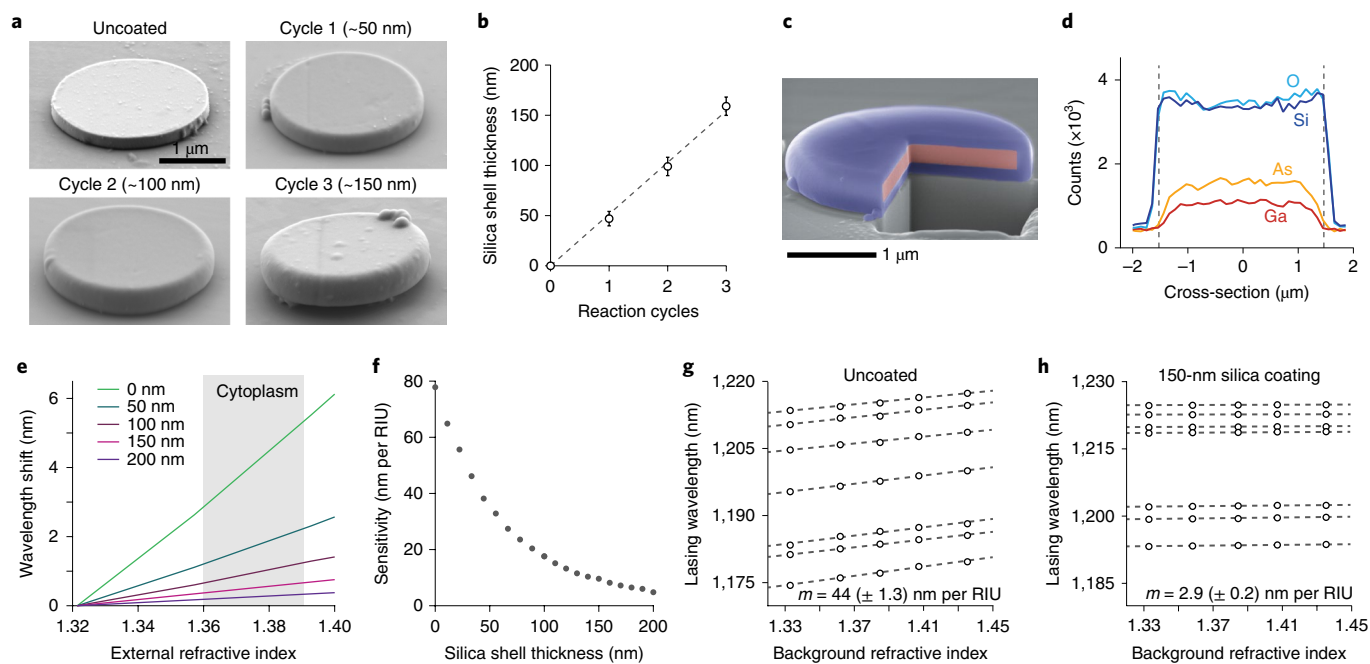


Fig. 3 | Silica coating of III–V semiconductor microdisk lasers. **a**, SEM images of microdisks before and after 1, 2 or 3 coating cycles. **b**, Silica shell thickness versus reaction cycles ($N \geq 9$ each). Mean \pm 95% confidence intervals (CI). **c**, False-colour cross-sectional SEM image of a coated microdisk cut with focused ion beam. **d**, Energy dispersive X-ray spectroscopy analysis of different elements along the diameter of a coated microdisk. **e**, Wavelength shift of a microdisk’s emission versus external refractive index, calculated from finite-difference time-domain simulations for increasing thicknesses of coating. The grey shaded region corresponds to the typical range for refractive index of cytoplasm. **f**, Sensitivity of the microdisk’s resonance to external refractive index as a function of coating thickness, calculated for small variations around $n_1 = 1.37$. **g, h**, Lasing wavelength versus background refractive index for uncoated (**g**) and 150-nm coated (**h**) microdisks on glass ($N = 7$ each). Empty circles are experimental data; dashed lines are linear fits.

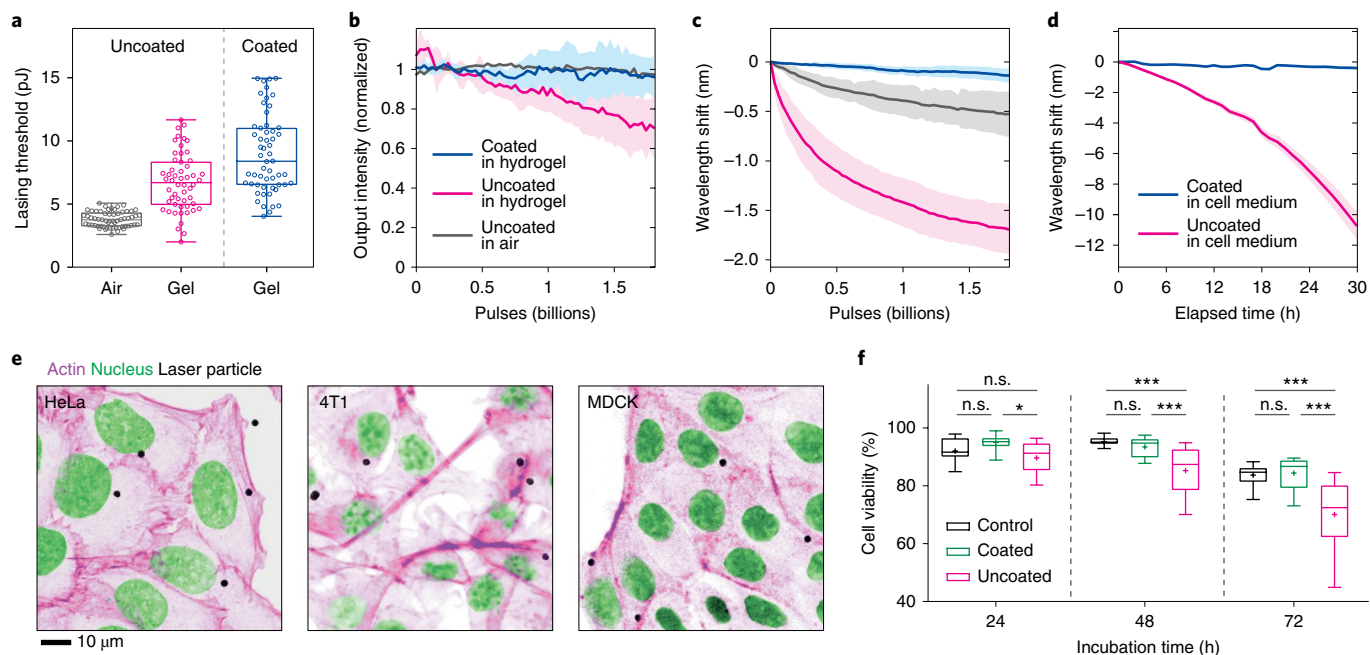


Fig. 4 | Stability and biocompatibility of LPs. **a**, Distribution of lasing thresholds for uncoated microdisks in air ($N = 60$), uncoated microdisks in Matrigel ($N = 54$) and coated microdisks in Matrigel ($N = 56$). **b, c**, Lasing output intensity (**b**) and resonance wavelength shift (**c**) of microdisks under continuous illumination up to 1.8 billion pump pulses ($N = 4$ each); solid lines are the mean and shaded regions are 95% CI. **d**, Long-term lasing-wavelength shifts of coated ($N = 51$) and uncoated microdisks ($N = 6$) on glass substrate in cell culture medium up to 30 h. Solid lines are the mean and shaded regions are 95% CI. **e**, Confocal fluorescence images of human cervical cancer (HeLa), mouse breast tumour (4T1) and canine kidney epithelial (MDCK-II) cells with staining for actin (magenta), and nucleus (green), overlaid with brightfield transmission images of LPs (greyscale). **f**, Cell viability of MDCK-II cells at 24 h, 48 h and 72 h after incubation with LPs. A two-way analysis of variance (ANOVA) was used for statistical analysis [$F(2,22) = 16.47$] ($*P < 0.01$, $***P < 0.001$; n.s., not significant).

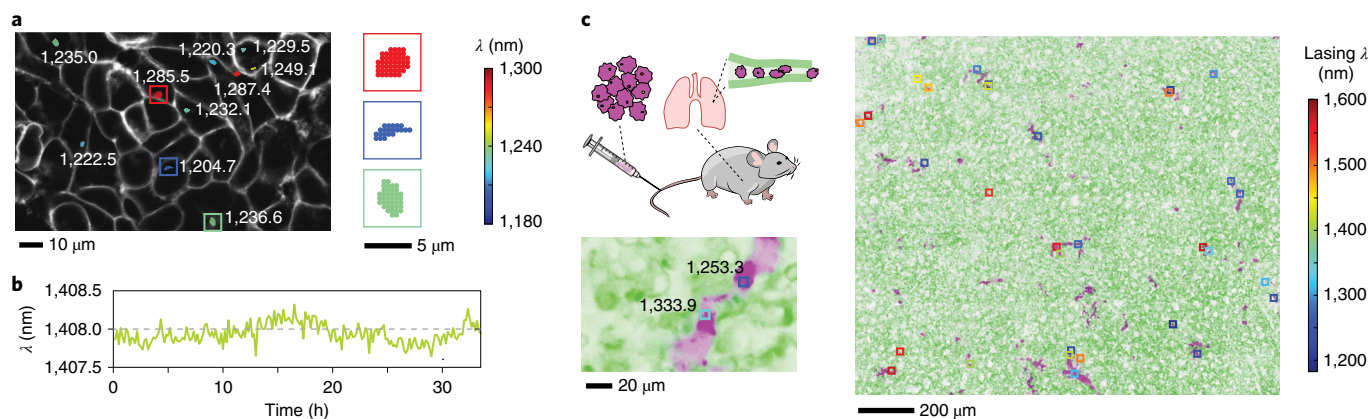


Fig. 5 | High-speed imaging and characterization of LPs as cell tagging probes. **a**, Overlaid LASE-fluorescence imaging of LPs inside membrane-GFP-expressing human embryonic kidney (HEK-293) cells. Inset, zoomed-in images of three LPs, in which the colour of each dot (pixel) represents the peak wavelength of laser emission. **b**, Representative wavelength trace of an intracellular LP measured every 10 min for 33 h. **c**, LP-tagged, fluorescence-dye-labelled 4T1 cells were injected intravenously into a live mouse. After 15 min, lung tissue was removed for ex vivo imaging. Maximum intensity z-projection images show administered 4T1 cells (purple), lung parenchyma (green), and the positions (squares) and wavelengths (colour) of LPs in the lung.

To assess the suitability of our LPs as intracellular probes, we performed time-lapse imaging to observe the migration and proliferation of MDCK-II cells containing LPs for several days (Supplementary Videos 2, 3). As cells divided, LPs were transmitted from a mother cell to daughter cells. Mitotic partitioning of multiple LPs tended to be asymmetric, fitting a skewed binomial probability distribution (Supplementary Fig. 7). Uptake statistics of LPs by MDCK cells after 24 h incubation for different initial concentrations are reported in Supplementary Fig. 8. For cells containing up to six particles, their presence did not much affect cell cycle times (Supplementary Fig. 8). A cell proliferation assay also revealed no significant difference in proliferation rate between cells with and without LPs ($P = 0.09$ at 48 h, $P = 0.35$ at 72 h; Supplementary Fig. 8). A few rare cells with an excessive number (>10) of particles were unable to complete mitosis and underwent apoptosis (Supplementary Video 3). We also performed a wound-healing assay on LP-tagged and untreated MDCK-II cells to confirm that internalized LPs had no appreciable effect on cell motility (Supplementary Fig. 8). Although this data suggests that coated LPs are biocompatible, further studies are needed to exclude any effect on specific cellular functions.

For long-term cell tracking, intracellular LP retention is important to be able to assign a LP unambiguously to a specific cell. Previous works have shown that for sub-micrometre particles the rate of exocytosis decreases with increasing particle size, irrespective of cell type³⁵. Particles of diameter 1–3 μm were found to remain internalized in cells for at least six days^{36,37}. We followed hundreds of LP-tagged MDCK-II cells in vitro using time-lapse imaging for over 60 h (Supplementary Videos 1–3) and did not observe any clear evidence of exocytosis (Supplementary Video 4). Although we cannot exclude the possibility of LPs being released after cell death, appropriate surface coatings may prevent their re-uptake³⁸.

Imaging of intracellular LPs

For high-speed imaging of LPs, we coupled the pump laser and spectrometer to a laser-scanning confocal microscope. The system can acquire the LASE images of LPs (at 100 μs per pixel) and the brightfield transmission and confocal fluorescence images of cells and tissues. For example, LASE-fluorescence microscopy showed signatures of individual LPs with varying shapes depending on their orientation inside the cytoplasm of HEK-293 cells expressing membrane-localized green fluorescent protein (GFP) (Fig. 5a).

Using a compact cell-culture incubator on the microscope, we acquired time-lapse LASE images of LPs inside cells. The LPs

were identified and tracked over time using an algorithm (see Methods) that exploits both positional and spectral information (Supplementary Note 2 and Supplementary Fig. 9). Tracking LP-tagged MDCK-II cells over 33 h in vitro showed that the output wavelengths of LPs in the cytoplasm were stable (Fig. 5b and Supplementary Fig. 10), apart from random fluctuations (0.1 nm) and slower variations. These changes were attributed to the residual sensitivity to the surrounding refractive index that changes slowly by natural cellular processes and rapidly by random-walk movement of LPs inside the cytoplasm. The wavelength variation exhibited a normal distribution with standard deviation $\sigma = 0.18$ nm. For LPs with nominal difference in wavelength of $\Delta = 1$ nm, this corresponds to an error probability in identifying LPs of $P \approx 10^{-4}$ (Supplementary Note 3). This error can be reduced by time-lapse spectral measurement averaging random fluctuations or adding redundancy such as positional information.

We then tested the possibility of tagging and imaging cells in tissues. 4T1 cells were stained with a fluorescent dye and loaded with LPs. They were then injected into the tail vein of a membrane-GFP-expressing mouse, in a model mimicking hematogenous micrometastasis. After 15 min, the lungs (where most of the injected cells are trapped) were explanted and imaged with our LASE system. Co-localization of LP emission with the cellular dye demonstrates their reliability as intracellular tags even in scattering tissues (Fig. 5c).

Longitudinal tracking in tumour spheroids

To demonstrate large-scale cell tracking, we used a three-dimensional tumour spheroid model using LP-tagged polyclonal 4T1 breast cancer cells. A single spheroid contained about 70,000 LPs. Using the LASE microscope setup described above, it took 47 min to acquire a z-stack over an imaging volume of $1 \times 1 \times 0.28$ mm³. A computer-automated three-dimensional scan was conducted every hour for 128 h, during which the spheroid expanded in size (Fig. 6a and Supplementary Video 5). At each time point, 4,500 to 8,000 LPs were detected, with a good uniformity in wavelength distribution across the 1,180–1,580 nm spectral range (Fig. 6b and Supplementary Fig. 11). The number of LPs detected increased over time, as the tumour grew toward the glass-bottomed plate and more LP-tagged cells entered the imaging volume (although some left the imaging volume). Post hoc analysis of fixed sections of the spheroid revealed that by the end of the experiment the average ratio of LPs per cell was about 0.6 (Supplementary Fig. 11), from which we

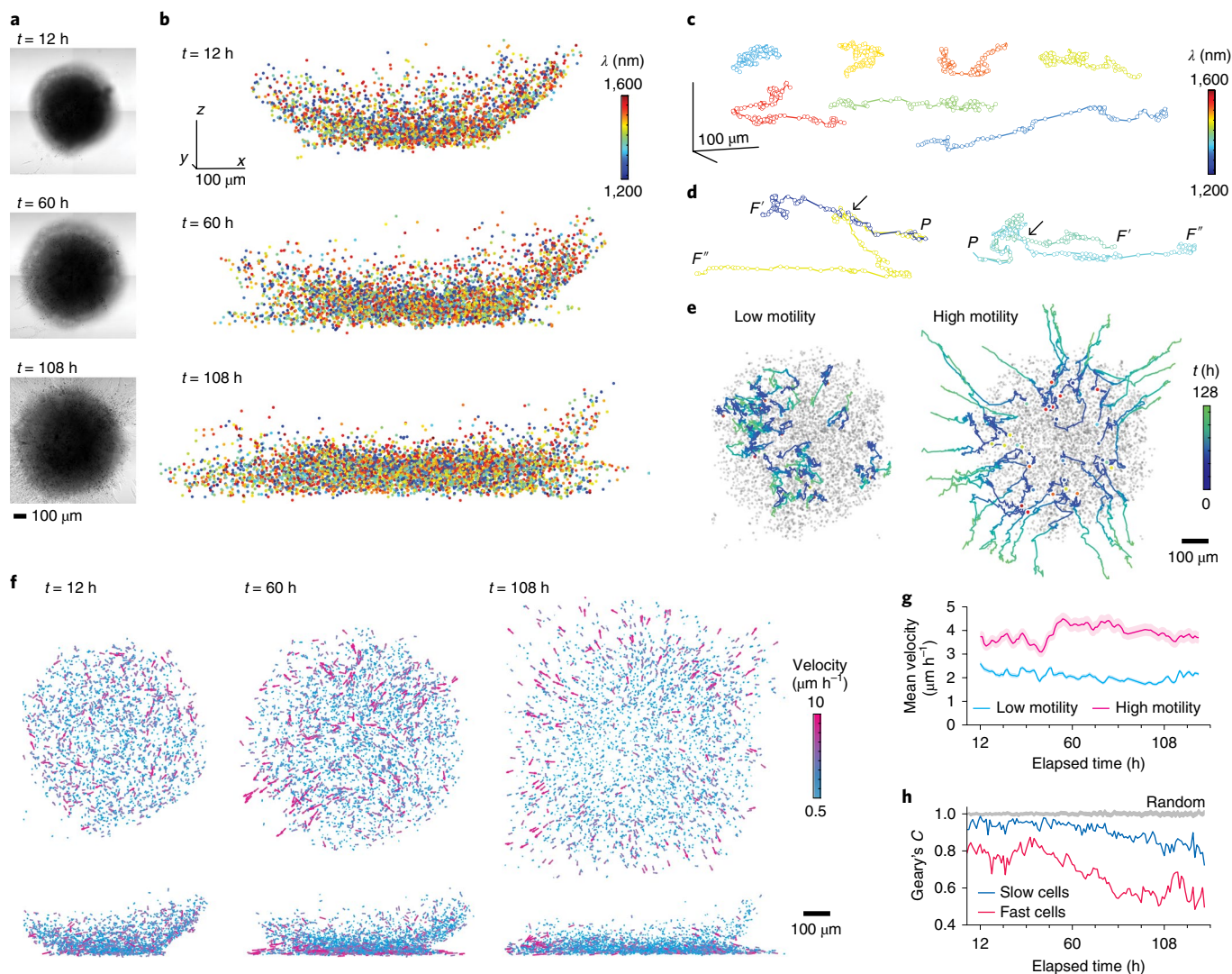


Fig. 6 | Cell tracking in a tumour spheroid. **a**, Optical transmission of the tumour spheroid at 12 h, 60 h and 108 h. **b**, Spatial distribution of LPs inside the tumour. Each dot represents a LP, with colour coding for its wavelength. **c**, Trajectories of exemplary LPs; circles indicate measured positions every hour. **d**, Trajectories of single parental cells (P) separating (arrow) into two descendant cells (F' and F''). **e**, Representative paths of cells divided by average motility: high (top 25%), and low (bottom 25%). Initial position of each LP is marked with a circle, colour-coded by wavelength; the path's colour denotes elapsed time over 128 h. Grey dots denote the positions of all LPs at 12 h. **f**, Maps of instantaneous velocities of tracked cells at different time points. **g**, Mean instantaneous velocities of cells in the high- and low-motility groups over time for cells tracked from 12 h to 120 h ($N=200$ each). The shaded region indicates 95% CI. **h**, Geary's coefficient for spatial correlation of cell velocities as a function of time for all tracked cells. Fast and slow cells represent the top and bottom 25% in instantaneous velocities at each time. A coefficient significantly <1 corresponds to high correlation, ≈ 1 corresponds to no correlation, and >1 corresponds to anti-correlation.

estimated that approximately 20% of the cells are tagged with LPs. Using our tracking algorithm, we were able to track 75–80% of all detected LPs for longer than 24 h, among which 731 were tracked for more than 125 h (Supplementary Fig. 11). To quantify cell motility, we used the position of the imaged LPs as a proxy for the location of the cells containing them. The 3D trajectories reveal a variety of migratory patterns (Fig. 6c). Long trajectories typically show several intermittently slow regions with an interval of about 1 day, which we hypothesize to result from cell division. We found groups of 2–3 LPs travelling in very close proximity, which we interpret as being inside the same cells (Supplementary Fig. 11). Some of the initially co-travelling LPs separated into two distinct paths (Fig. 6d). This phenomenon is probably due to splitting of particles into different descendant cells during cell division.

The longitudinal tracking data permitted various single-cell analyses and grouping in terms of behavioural phenotypes. We classified

cells depending on their average motility (that is, the ratio of travel distance to the tracking duration; see Supplementary Fig. 12). While the low-motility group ($<25\%$) cells were found to remain in the core of the spheroid, the trajectories of the high-motility group ($>75\%$) cells feature outward migratory behaviour and invasion into the surrounding gel matrix, particularly along paths near the glass plate (Fig. 6e). These two functionally distinct groups appeared to have originated from statistically distinctive regions in the tumour at early times (Supplementary Fig. 12). From the trajectory of each cell in every 6-h window, the instantaneous velocity was calculated, and velocity maps at each time were obtained (Fig. 6f). The time-lapse video of the velocity maps shows how individual cells move during spheroid growth and invasion (Supplementary Video 6). Interestingly, the high-motility cells had consistently higher speeds than low-motility cells throughout the entire duration and underwent moderate acceleration at 40–60 h at the onset of invasion

(Fig. 6g). In terms of instantaneous velocity, fast and slow cells (top and bottom quartile) were analysed at each time point. A Geary's coefficient analysis showed significantly higher spatial correlation of velocities among the fast cells compared to the slow cells and a randomized control, suggesting the presence of non-cell-autonomous behaviours (Fig. 6h). In particular, strong spatial correlation at earlier time points (20–40 h) is attributed to the streams of cells moving in small packs within the spheroid (Supplementary Fig. 12). These results demonstrate the novel capability of gathering large-scale longitudinal single-cell information in situ using LPs.

Discussion

We have demonstrated that thickly coated semiconductor microdisks are well suited for cell tagging and tracking applications owing to their low pump energy, excellent stability and biocompatibility. With respect to the spontaneous emission typical of fluorophores, the stimulated emission from single-mode microlasers has several distinct characteristics, such as coherent-state statistics, sharp threshold and picosecond-scale decay times, that are potentially useful for imaging and sensing^{39,40}.

Most remarkably, the spectral width of laser emission is 100 times narrower than that of typical fluorophores. We have harnessed this property for wavelength-encoded tagging and tracking of thousands of densely populated cells in a three-dimensional scattering tissue. The spectral encoding offers a compelling advantage for cell identification and tracking, compared to image-based tracking (such as by light-sheet microscopy) which requires frequent imaging (every few minutes)⁴¹.

Improvements in multiplexing capability are possible. First, the total wavelength span could be expanded to the NIR-I and visible range using appropriate group III–V and group II–VI semiconductor materials. Second, when multiple LPs with different wavelengths are combined, the number of unique identifiers scales as $\frac{N!}{(N-m)!m!}$

where N is the number of colours for singlet LPs ($m=1$) and m is the number of particles in the multiplet. With $N=1,000$, doublets ($m=2$) can have half a million identifiers, and the number increases to 166 million for triplets ($m=3$). Preliminary results showed promising feasibility of this massively scalable approach (Supplementary Fig. 13).

Recent work has highlighted the importance of cellular heterogeneity at the single-cell level⁴². Whereas current understanding primarily stems from sequencing of single dissociated cells, emerging spatial transcriptomic techniques promise understanding of cellular identity in the tissue context⁴³. Laser-particle-enabled cell tagging could allow sorting and extraction of cells of interest for post hoc analyses such as flow cytometry or single-cell sequencing⁴⁴. Furthermore, it can enable highly multiplexed cell tracking of individual cells, offering rich complementary information on cellular behaviour, including migration, motility, cell–cell interactions and spatial clustering. The combination of imaging, single-cell tracking, transcriptomic and proteomic assays will enable unprecedentedly comprehensive evaluation of cell identity and function.

Online content

Any methods, additional references, Nature Research reporting summaries, source data, statements of code and data availability and associated accession codes are available at <https://doi.org/10.1038/s41566-019-0489-0>.

Received: 7 October 2018; Accepted: 6 June 2019;

Published online: 22 July 2019

References

- Johnson, B. E. et al. Mutational analysis reveals the origin and therapy-driven evolution of recurrent glioma. *Science* **343**, 189–193 (2014).
- Wagenblast, E. et al. A model of breast cancer heterogeneity reveals vascular mimicry as a driver of metastasis. *Nature* **520**, 358–362 (2015).

- Klein, A. M. M. et al. Droplet barcoding for single-cell transcriptomics applied to embryonic stem cells. *Cell* **161**, 1187–1201 (2015).
- Montoro, D. T. et al. A revised airway epithelial hierarchy includes CFTR-expressing ionocytes. *Nature* **560**, 319–324 (2018).
- Nguyen, L. V. et al. Barcoding reveals complex clonal dynamics of de novo transformed human mammary cells. *Nature* **528**, 267–271 (2015).
- Bhang, H. C. et al. Studying clonal dynamics in response to cancer therapy using high-complexity barcoding. *Nat. Med.* **21**, 440–448 (2015).
- Rompolas, P. et al. Live imaging of stem cell and progeny behaviour in physiological hair-follicle regeneration. *Nature* **487**, 496–499 (2012).
- Weï, L. et al. Super-multiplex vibrational imaging. *Nature* **544**, 465–470 (2017).
- Livet, J. et al. Transgenic strategies for combinatorial expression of fluorescent proteins in the nervous system. *Nature* **450**, 56–62 (2007).
- Lin, C. et al. Submicrometre geometrically encoded fluorescent barcodes self-assembled from DNA. *Nat. Chem.* **4**, 832–839 (2012).
- Rees, P. et al. Nanoparticle vesicle encoding for imaging and tracking cell populations. *Nat. Methods* **11**, 1177–1181 (2014).
- Vahala, K. J. Optical microcavities. *Nature* **424**, 839–846 (2003).
- Humar, M. & Yun, S. H. Intracellular microlasers. *Nat. Photonics* **9**, 572–576 (2015).
- Schubert, M. et al. Lasing within live cells containing intracellular optical microresonators for barcode-type cell tagging and tracking. *Nano Lett.* **15**, 5647–5652 (2015).
- Martino, N. et al. Dense-wavelength-division laser micro-particles: fabrication and imaging in tissues. In *Conference on Lasers and Electro-Optics SW3J.4* (Optical Society of America, 2018).
- Fikouras, A. H. et al. Non-obstructive intracellular nanolasers. *Nat. Commun.* **9**, 4817 (2018).
- Li, E. H. Material parameters of InGaAsP and InAlGaAs systems for use in quantum well structures at low and room temperatures. *Phys. E* **5**, 215–273 (2000).
- Smith, A. M., Mancini, M. C. & Nie, S. Bioimaging: second window for in vivo imaging. *Nat. Nanotechnol.* **4**, 710–711 (2009).
- Hong, G., Antaris, A. L. & Dai, H. Near-infrared fluorophores for biomedical imaging. *Nat. Biomed. Eng.* **1**, 0010 (2017).
- Foreman, M. R., Swaim, J. D. & Vollmer, F. Whispering gallery mode sensors. *Adv. Opt. Photonics* **7**, 168–240 (2015).
- Zhang, Z. et al. Visible submicron microdisk lasers. *Appl. Phys. Lett.* **90**, 111119 (2007).
- Frateschi, N. C. & Levi, A. F. J. The spectrum of microdisk lasers. *J. Appl. Phys.* **80**, 644–653 (1996).
- Andronico, A. et al. Semiconductor microcavities for enhanced nonlinear optics interactions. *J. Eur. Opt. Soc. Rapid Publ.* **3**, 08030 (2008).
- Kohl, P. A. Photoelectrochemical etching of semiconductors. *IBM J. Res. Dev.* **42**, 629–638 (1998).
- Gil-Santos, E. et al. Scalable high-precision tuning of photonic resonators by resonant cavity-enhanced photoelectrochemical etching. *Nat. Commun.* **8**, 14267 (2017).
- Liu, B. S. & Han, M. Synthesis, functionalization, and bioconjugation of monodisperse, silica-coated gold nanoparticles: robust bioprobes. *Adv. Funct. Mater.* **15**, 961–967 (2005).
- Choi, W. et al. Tomographic phase microscopy. *Nat. Methods* **4**, 717 (2007).
- Intonti, F. et al. Mode tuning of photonic crystal nanocavities by photoinduced non-thermal oxidation. *Appl. Phys. Lett.* **100**, 033116 (2012).
- Schöttler, S. et al. Protein adsorption is required for stealth effect of poly(ethylene glycol)- and poly(phosphoester)-coated nanocarriers. *Nat. Nanotechnol.* **11**, 372–377 (2016).
- Kim, J., Piao, Y. & Hyeon, T. Multifunctional nanostructured materials for multimodal imaging, and simultaneous imaging and therapy. *Chem. Soc. Rev.* **38**, 372–390 (2009).
- Kumar, R. et al. In vivo biodistribution and clearance studies using multimodal organically modified silica nanoparticles. *ACS Nano* **4**, 699–708 (2010).
- Patiño, T., Soriano, J., Barrios, L., Ibáñez, E. & Nogués, C. Surface modification of microparticles causes differential uptake responses in normal and tumoral human breast epithelial cells. *Sci. Rep.* **5**, 11371 (2015).
- Conner, S. D. & Schmid, S. L. Regulated portals of entry into the cell. *Nature* **422**, 37–44 (2003).
- Zhang, T. et al. Cellular effect of high doses of silica-coated quantum dot profiled with high throughput gene expression analysis and high content cellomics measurements. *Nano Lett.* **6**, 800–808 (2006).
- Chithrani, B. D. & Chan, W. C. W. Elucidating the mechanism of cellular uptake and removal of protein-coated gold nanoparticles of different sizes and shapes. *Nano Lett.* **7**, 1542–1550 (2007).
- Sarkar, D., Ankrum, J. A., Teo, G. S. L., Carman, C. V. & Karp, J. M. Cellular and extracellular programming of cell fate through engineered intracrine-, paracrine-, and endocrine-like mechanisms. *Biomaterials* **32**, 3053–3061 (2011).
- Serda, R. E. et al. Mitotic trafficking of silicon microparticles. *Nanoscale* **1**, 250–259 (2009).

38. Xie, J., Xu, C., Kohler, N., Hou, Y. & Sun, S. Controlled PEGylation of monodisperse Fe₃O₄ nanoparticles for reduced non-specific uptake by macrophage cells. *Adv. Mater.* **19**, 3163–3166 (2007).
39. Cho, S., Humar, M., Martino, N. & Yun, S. H. Laser particle stimulated emission microscopy. *Phys. Rev. Lett.* **117**, 193902 (2016).
40. Vollmer, F. & Arnold, S. Whispering-gallery-mode biosensing: label-free detection down to single molecules. *Nat. Methods* **5**, 591–596 (2008).
41. Richards, R., Mason, D., Levy, R., Bearon, R. & See, V. 4D imaging and analysis of multicellular tumour spheroid cell migration and invasion. Preprint at <https://www.biorxiv.org/content/10.1101/443648v1> (2018).
42. Tanay, A. & Regev, A. Scaling single-cell genomics from phenomenology to mechanism. *Nature* **541**, 331–338 (2017).
43. Wang, X. et al. Three-dimensional intact-tissue sequencing of single-cell transcriptional states. *Science* **361**, eaat5691 (2018).
44. Kalhor, R. et al. Developmental barcoding of whole mouse via homing CRISPR. *Science* **361**, eaat9804 (2018).

Acknowledgements

This work was supported by the US National Institutes of Health (NIH) grants DP1-OD022296, P41-EB015903, R01-CA192878, and National Science Foundation (NSF) grants ECCS-1505569. Electron microscopy was performed in the Microscopy Core of the Center for Systems Biology/Program in Membrane Biology, which is partially supported by an Inflammatory Bowel Disease Grant DK043351 and a Boston Area Diabetes and Endocrinology Research Center (BADERC) Award DK057521. This research used the resources of the Center for Functional Nanomaterials, which is a US Department of Energy Office of Science User Facility, at Brookhaven National Laboratory under contract number DE-SC0012704 and of the Center for Nanoscale Systems, part of Harvard University, a member of the National Nanotechnology Coordinated Infrastructure Network (NNCI), which is supported by the NSF under award number 1541959. We thank V. Vinarsky and D. Montoro for their comments, and F. Camino for helping with focused ion beam measurements.

Author contributions

S.-H.Y., N.M. and S.J.J.K. conceived and designed the project. N.M., H.J., H.-M.K., Y.-H.L. and S.-H.Y. designed microdisks. N.M. and A.C.L. fabricated microdisks. N.M. and S.J.J.K. developed the microdisk transfer protocol. S.J.J.K. and S.J.W. developed and performed silica coating of microdisks. N.M. and A.C.L. conducted theoretical simulations. S.J.J.K., S.F. and S.-J.J. performed cell cultures and biocompatibility assays. N.M. and J.W. designed the LASE microscope system. N.M. and S.J.J.K. performed and analysed optical characterization and imaging of LPs. S.J.J.K. and S.-J.J. performed ex vivo lung imaging. S.J.J.K., A.C.L., S.F., S.-J.J. and P.H.D. analysed time-lapse videos of intracellular LPs. N.M., S.J.J.K., A.C.L. and S.-H.Y. prepared figures and wrote the manuscript with input from all authors.

Competing interests

The authors declare the following competing interests: S.-H.Y. holds patents on technologies related to the devices developed in this work. S.-H.Y. and S.J.J.K. have financial interests in LASE Innovation Inc., a company focused on commercializing technologies based on LPs, for a variety of applications in life science and healthcare. S.-H.Y.'s interests were reviewed and are managed by Massachusetts General Hospital and Partners HealthCare in accordance with their conflict of interest policies.

Additional information

Supplementary information is available for this paper at <https://doi.org/10.1038/s41566-019-0489-0>.

Reprints and permissions information is available at www.nature.com/reprints.

Correspondence and requests for materials should be addressed to S.-H.Y.

Publisher's note: Springer Nature remains neutral with regard to jurisdictional claims in published maps and institutional affiliations.

© The Author(s), under exclusive licence to Springer Nature Limited 2019

Methods

Fabrication. Microdisk resonators were fabricated starting from wafers composed of an InP substrate and two epitaxial layers: a 200-nm-thick active layer of lattice-matched, undoped InGaAsP or InAlGaAs and a 100-nm-thick capping layer of (undoped) InP. The capping layer was introduced to protect the active layer during the reactive ion etching (RIE) process.

For optical lithography samples, 2 μm of SU-8 photoresist (MicroChem) was spin-coated on cleaned wafers and then soft-baked (1 min at 65 °C, 2 min at 90 °C, 1 min at 65 °C). The mask used for photolithography (chrome on quartz, Benchmark Technologies) had a hexagonal pattern of holes (2.5 μm in diameter, spaced by 6 μm) with a density of 3.2 million microdisks per square centimetre. After the photoresist deposition, the wafer was diced into squares of 5 mm \times 10 mm to produce about a million microdisks per batch. Photolithography consisted of exposure of the i- and h-line of a mercury arc lamp at a total dose of 40–60 mJ cm⁻² (Karl Suss MJB4 mask aligner), a post-exposure bake at 90 °C, development in SU-8 Developer (MicroChem), and rinsing in isopropyl alcohol. A hard-baking step at 200 °C was performed to harden the SU-8 pattern and smooth its surface, followed by a desmum step in O₂ plasma (30 sccm, 100 W for 3 min) to remove photoresist residues (Anatech Barrel SCE 160). For dry etching, inductively coupled plasma reactive ion etching (ICP-RIE) (Unaxis Shuttleline) was conducted using hydrogen bromide chemistry, which resulted in an etching depth of about 700 nm. After RIE, the photoresist was removed by mechanical scrubbing with cleanroom foam swabs, and the sample was rinsed in acetone, isopropyl alcohol and de-ionized water. A second O₂ plasma treatment and an immersion in the polymer stripper PRS-3000 (J.T. Baker) were performed to further remove residues.

For electron-beam lithography samples, the semiconductor wafer was first coated with 330 nm of SiO₂ by plasma-enhanced chemical vapour deposition (Orion III, Trion) to serve as a hard mask for the semiconductor etching process. Circular patterns of the desired dimensions were defined by 100-keV electron-beam lithography (JBX6300-FS, JEOL) on a negative-tone resist (ma-N 1410, MicroChem), and transferred to the silica hard mask by ICP-RIE (Plasmalab 100, Oxford Instruments) using fluoroform chemistry. A second etching step based on silicon-tetrachloride was used to transfer the pattern to the semiconductor. The remaining SiO₂ hard mask was removed with a final fluoroform-based RIE step.

Transfer and silica coating. For characterization in air, the post-RIE samples were partially wet-etched in a 3:1 solution of HCl in de-ionized water for 5–10 s, leaving the microdisks suspended on a small pillar. To completely detach the microdisks, the substrates were wet-etched face down in the HCl:H₂O solution inside a 5-ml centrifuge tube for 30 s. The suspension of microdisks was then transferred to a 1- μm -pore centrifuge filter, and filtered thoroughly by at least three repeated cycles of centrifugation and resuspension (via ultrasonication) using ultrapure water or ethanol. The sample collection efficiency transferring from substrate to solution was typically around 50%.

Silica coating of the microdisks was performed by multiple cycles of a modified Stöber process. In a typical reaction cycle, microdisks (about 10⁶ disks per ml) were suspended in 670 μl of an ethanol:H₂O solution (80 v/v% ethanol). Next, 60 μl of 40 mM tetraethyl orthosilicate (TEOS) in ethanol, and 45 μl of ammonium hydroxide solution (28 v/v% NH₄OH) were added, and the microdisk solution was shaken vigorously at 1,400 r.p.m. for 6 h at room temperature. To harden the silica shell to improve chemical stability, the temperature was increased to 80 °C and the solution was kept mixing for at least 12 h (ref. 45). Following each coating reaction, the microdisks were thoroughly centrifuge-filtered and resuspended in water or ethanol. Multiple cycles of coating results in occasional (<10%) formation of LP multiplet aggregates. To fabricate a fluorescein-doped silica shell, fluorescence isothiocyanate (FITC) was reacted with 3-aminopropyl-trimethoxysilane (APTMS) and the resulting conjugate, FITC-APTMS, was used instead of TEOS in the coating reaction.

Surface functionalization was conducted by reacting coated microdisks with silane reagents. Coated microdisks in 600 μl of water (about 10⁵ microdisks per ml) were mixed with 60 μl of 20 mM silane-polyethylene glycol-FITC (5 kDa) or silane-polyethylene glycol-biotin (5 kDa) in water, 6 μl of 20 mM TEOS in ethanol, and 4 μl of ammonium hydroxide solution (28 v/v% NH₄OH). The solution was mixed at 1,400 r.p.m. at 70 °C for 3 h, and then kept mixing at room temperature for at least 12 h, before centrifuge filtration and resuspension.

Samples embedded in three-dimensional hydrogel matrix were prepared by mixing equal volumes of an aqueous solution of microdisk LPs (coated or uncoated) with Matrigel (Corning) and incubating for 2 h at 37 °C to allow matrix cross-linking. For cell experiments, LPs were resuspended in sterile filtered de-ionized water before adding to cells.

Modelling of microdisk resonance. Theoretical modelling of uncoated microdisk resonances for different diameters and external refractive indexes was performed as described in Supplementary Note 1 with a custom MATLAB script. Modelling of microdisk resonance sensitivity for different silica-coating thicknesses was conducted via a series of fully three-dimensional finite-difference time-domain simulations (Lumerical FDTD solutions). The semiconductor microdisk was modelled as a cylinder of refractive index of 3.445, while the refractive index of the

silica shell was taken from tabulated values in ref. 46. The simulation region was set with perfectly matched layer boundary conditions on all directions. The distance to the perfectly matched layer boundaries as well as the meshing size were chosen after a series of convergence tests. The optical modes supported by the resonator were excited by a number of randomly placed in-plane dipole emitters, and the resonance wavelength at the bandwidth of interest was recorded as the background refractive index of the simulation was varied.

Electron microscopy. 10 μl of LP suspensions in water were added and air-dried on silicon wafer chips for SEM, and on formvar-carbon-coated nickel mesh grids (Electron Microscopy Sciences) for transmission electron microscopy (TEM). TEM images were obtained using a JEOL JEM 1011 microscope at 80 kV. SEM characterization was performed on a Hitachi S-4800 microscope and a Zeiss Ultra Plus Field-Emission microscope at 2 keV. For cross-sectional viewing, coated microdisks were first milled with a focused Ga⁺ beam using a dual-beam SEM/focused-ion-beam tool (Helios Nanolab, FEI Company). Energy-dispersive X-ray spectroscopy and mapping was performed on a Zeiss Supra55VP field emission microscope at 8 keV.

Optical characterization. For optical characterizations and imaging of LPs, a commercial laser-scanning confocal microscope (Olympus FV3000) was modified. A pump laser (Spectra Physics VGEN-ISP-POD, 1,060–1,070 nm, pulse duration 3 ns, repetition rate 2 MHz) was coupled to a side port of the laser-scanning unit of the microscope. The emission from LPs was collected from the same port and relayed by a dichroic mirror to a near-infrared spectrometer using an InGaAs linescan camera (Sensor Unlimited 2048 L), operated with an integration time of 1 ms for high-resolution characterization; for LASE imaging, the acquisition of spectrometer data was performed at 100 μs integration and synchronized to the laser-scanning unit. A grating with 600 lines per millimetre was used for high-resolution characterization (0.2 nm resolution, 150 nm span). For LASE imaging, a grating with 200 lines per millimetre (0.6-nm resolution over 1,150–1,600 nm) was used. A near-infrared-optimized, 20 \times , 0.45-NA (numerical aperture) objective (Olympus IMS LCPLN20XIR) was used for LASE microscopy. The pump beam under-filled the objective lens (20 \times) such that the focal beam size was 2 μm , matching the size of LPs. Confocal fluorescence images were acquired with a 40 \times , 0.7-NA objective (Olympus LUCPLFLN40X). A stage-top incubator (Tokai Hit) kept the samples at 37 °C and 5% CO₂ during imaging.

Stability of LP emission was performed in air for uncoated microdisks and in hydrogel for both coated and uncoated microdisks. LPs were pumped with $E_p = 40$ pJ per pulse at 2 MHz repetition rate. For continuous pumping, spectra from individual LPs were collected for 15 min every 15 s. For long-term stability, emission was collected via LASE imaging every hour for 30 h. The output intensity and wavelength were determined from the area under the spectral curve and the Gaussian-fit centre respectively.

The sensitivity of LP emission to external refractive index was measured in different sucrose solutions prepared with concentrations of 0, 20, 38, 50 and 64% w/w. Their refractive index was measured using a portable refractometer (PAL-RI, ATAGO). Uncoated and coated (150 nm) LPs were deposited on different wells of a glass-bottom 96-well plate. For each concentration, 300 μl of sucrose solution was pipetted into each well and a LASE image was acquired. Between successive measurements, the wells were washed twice with ultra-pure water. We note that under this experimental arrangement, only the refractive index of the top half-space is varied, while the bottom half remains constant throughout (glass).

Cell culture and biocompatibility experiments. HeLa human cervical cancer cells (ATCC), 4T1 mouse breast tumour cells (ATCC) and MDCK-II canine kidney epithelial cells (ECACC) were cultured and maintained in serum-supplemented cell media following the manufacturer's guidelines. Membrane-GFP-expressing HEK-293 human embryonic kidney cells were a gift from A. E. Cohen, and were cultured in Dulbecco's modified Eagle medium (DMEM) supplemented with 10% (v/v) foetal bovine serum (FBS) and 1% (v/v) penicillin-streptomycin. Cells were stained after fixation with AlexaFluor 594-Phalloidin for actin (Thermo Fisher), and DAPI for nucleus (ProLong Gold AntiFade Mountant with DAPI, Thermo Fisher) following the manufacturer's guidelines.

A typical protocol for loading LPs into cells is as follows. Cells were plated in their respective media at a known density in a glass-bottomed, 96-well plate. Laser particles were resuspended in sterile filtered de-ionized water, and counted using a standard hemocytometer. The LP solution was then added to cells, at initial particle-to-cell ratios from 1:1 to 4:1. Immediately afterwards, the requisite amount of 10 \times PBS was added to maintain isotonicity. The dilution of cell media with addition of LP solution was <10%. The cell media was exchanged to fresh media within 2 h. Cells were then incubated at 37 °C and 5% CO₂ for 24–48 h until LP uptake was complete.

Cellular viability was assessed via a calcein-AM/ethidium homodimer-1 fluorescent assay (LIVE/DEAD viability/cytotoxicity kit, Thermo Fisher). MDCK-II cells were switched to serum-free MEM- α for the duration of the experiment (up to 72 h) to minimize cell proliferation. Uncoated or coated microdisks in water were added to MDCK-II cells such that the particle-to-cell ratio was approximately 1:1. Fluorescent staining was conducted after 24 h, 48 h

and 72 h later. Fluorescence and bright-field microscopy was conducted to quantify particle uptake and cell viability (Keyence BZ-X700 microscope).

Cellular proliferation was assessed via a cell counting kit-8 (CCK, Millipore Sigma). After MDCK-II cells were plated, low (4:1 particle-to-cell) and high (32:1) concentrations of microdisks were added as previously described. CCK-8 staining was conducted at 48 and 120 h, when cells were approximately 80% confluent. Absorbance measurements were taken using a spectrophotometer (Epoch 2, BioTek Instruments).

Wound healing assay. MDCK-II cells were incubated with and without LPs at an initial LPs-to-cell concentration of 4:1. After 24 h, the cells were detached and plated into each chamber of a wound-healing assay insert (20,000 cells per well; culture-insert 2 well, ibidi). After 12 h, the inserts were removed. Time-lapse brightfield imaging was performed every 30 min on two inserts with LP-tagged cells and two controls. For each insert, we imaged and analysed five different areas of the closing gap. The images were segmented with Fiji and the cell-free area was computed for each time point.

Time-lapse bright-field imaging. To observe the internalization and interaction of cells with LPs, we used an automated, time-lapse, bright-field microscope (Keyence BZ-X700). MDCK-II cells were plated with LPs (particle-to-cell ratio of 2:1) in a 96-well glass-bottomed plate as described earlier. Images from different wells were taken every 5 min over a 60-h period in a stage-top incubator (Tokai Hit) at 37 °C and 5% CO₂. After correcting for drift artefacts, the processed videos were analysed frame-by-frame to record instances of particle uptake, cell division, and suspected exocytosis events. Over 400 individual cell cycles were annotated, from which we calculated the cell cycle time as a function of particle number, and the statistics of particle partitioning due to cell division. Empirical probabilities for LP partitioning were fitted with an asymmetric binomial distribution: $P(r) = C(n, r)p^r(1-p)^{n-r}$, where n is the number of particles in the parent cell, r is the number of particles in the daughter cell, $C(n, r) = \frac{n!}{r!(n-r)!}$, and n is a fitting parameter that quantifies the asymmetry of the distribution ($n = 0.5$ for a symmetric binomial distribution).

Ex vivo lung imaging. The MGH Institutional Animal Care and Use Committee approved our animal protocol (2017N000021) in accordance with NIH guidelines. Membrane-GFP-expressing ROSA^{mt/mG} mice (<https://www.jax.org/strain/007576>) were purchased from Jackson Laboratories. 4T1 cells were loaded with LPs in vitro as previously described, and stained with CellTracker Red (Thermo Fisher) following the manufacturer's guidelines. Approximately 2×10^5 4T1 cells containing around 1×10^5 LPs in 200 μ l of DPBS solution were injected intravenously into the tail vein of a membrane-GFP-expressing adult mouse under anaesthesia. After 30 min, the animal was euthanized and the lung was explanted. The entire lung was immersed in DPBS and placed on a glass-bottom dish. A 60 \times , 1.2-NA objective (Olympus UPLSAPO 60XW) was used for confocal fluorescence and LASE imaging up to 150 μ m in depth. For large-area imaging, 64 adjacent areas, each spanning $212 \times 212 \times 3 \mu\text{m}^3$ were imaged and stitched together in post-processing using Fiji and MATLAB.

Spheroid invasion assay. Approximately 1.5×10^5 LPs were added to 5×10^3 4T1 cells as previously described and incubated for 48 h until confluent in a 96-well cell-culture plate, to ensure complete uptake of LPs. Cells were transferred to an ultralow-attachment-coated round-bottom microplate (CellCarrier) to form spheroids. Each well initially contained approximately 2×10^4 cells and 7×10^4 LPs. After three days of incubation, the spheroids were transferred to a glass-bottomed microplate in 100 μ l of serum-supplemented cell media mixed with 100 μ l of Matrigel (Corning). After this passage, eventually extracellular LPs are left in the original plate. After 2 h, an additional 100 μ l of cell media was added. The spheroids were used for LASE imaging after 6 h. The spheroid was imaged every hour for a total of 129 measurements ($t = 0, 1, \dots, 128$ h). The imaged region was divided into four adjacent areas acquired sequentially; each area was $480 \times 480 \times 280 \mu\text{m}^3$ and was imaged at $320 \times 320 \times 70$ pixels, for 100 μ s per pixel; total imaging time for each scan was about 48 min (about 12 min per area). Laser pumping was set at $E_p = 80$ pJ per pulse.

LASE imaging data analysis. A custom Python software was used to analyse the spectra acquired during LASE imaging in real time, recording the data only when they contained peaks greater than a threshold level. Post-processing of the data was performed with a MATLAB custom code. The recorded spectra were further reduced to wavelength peaks by Gaussian fitting, producing a set of wavelength

(λ) and position (\mathbf{r}) data of each recorded 'lasing' event (or pixel). Since many lasing events can be recorded from a single LP, a clustering algorithm was applied to group the data from the same LP. A three-step hierarchical clustering algorithm was used: (1) clustering by position to isolate spatially separate clusters of lasing pixels; (2) clustering by wavelength to distinguish any adjacent particles with different wavelengths; and (3) clustering by position again to separate clusters in the cases where two particles with similar wavelengths were bridged by a third particle with a different emission. Once clusters are identified, their centroid position and mean wavelength were computed to represent corresponding LPs.

For particle-in-cell tracking, a metric (D_{ij}) was introduced, which represents a 'distance' between two particles identified in two separate measurements in four-dimensional space of wavelength (λ) and position (\mathbf{r}); the distance D_{ij} between the i th particle in an image and the j th particle in a preceding image is defined as: $D_{ij} = \left(\frac{|\lambda_i - \lambda_j|}{\Delta\lambda_0} \right)^4 + \left(\frac{|\mathbf{r}_i - \mathbf{r}_j|}{\Delta r_0} \right)^4$, where $\Delta\lambda_0$ and Δr_0 are adjustable parameters; we set $\Delta\lambda_0 = 1$ nm, whereas $\Delta r_0 = \sqrt{2D\Delta t}$, as an estimate of the expected maximum displacement for a LPs in the time interval Δt between the analysed frames ($D = 200 \mu\text{m}^2 \text{h}^{-1}$ in the spheroid tracking experiment). For each time point t_m , the distance D_{ij} of all imaged particles ($i = 1$ to N_m) from those ($j = 1$ to N_{m-1}) detected in the previous time (t_{m-1}) were calculated. Pairs of particles with a distance smaller than a threshold $D_{th} = 2$ were matched, starting from the one with the smallest distance. For the remaining particles, the matching procedure was repeated with the particles detected at earlier times (t_{m-2} , t_{m-3} , and t_{m-4}).

LPs within the same cell were identified by computing for each couple i, j of tracked particles their average (geometric) distance $\bar{s}_{ij} = \frac{1}{N_i} \sum_{t=t_0}^h \sqrt{|\mathbf{r}_i(t) - \mathbf{r}_j(t)|}$ at each time point. Particles with $\bar{s}_{ij} < 21 \mu\text{m}$ were considered as belonging to the same cell for the entire duration of the tracking and were thus merged in a single trace.

To remove the contribution of intracellular movements of LPs on the overall cellular trajectories, we applied a 6-h moving average to the tracked pathways.

Statistics. Data were presented as either box and whisker plots, or as mean and 95% confidence interval. Statistical hypothesis testing for the biocompatibility assays was done using either one-way or two-way analysis of variance (ANOVA), and all F -statistics were reported. Statistical significance was set at $\alpha = 0.05$. Post hoc comparisons were conducted using Tukey's test. Statistical analyses were performed using GraphPad Prism and MATLAB.

To quantify spatial autocorrelation in the spheroid tracking experiment, we computed Geary's coefficient as follows: $C = \frac{(N-1) \sum_i \sum_j \omega_{ij} |x_i - x_j|^2}{2W \sum_i |x_i - \bar{x}|^2}$, where N is the

number of neighbouring cells, and ω_{ij} is a spatial weight matrix that defines the neighbourhood region of interest, or the pack size of spatially correlated cells. A coefficient significantly < 1 corresponds to high correlation, ≈ 1 corresponds to no correlation, and > 1 corresponds to anti-correlation. Before normalization, ω_{ij} contains zeros on the diagonals and ones for neighbouring cells within a given distance. This distance is set to 60 μ m in Fig. 6h, and is varied from 30 μ m to 600 μ m in Supplementary Fig. 12c,e. The matrix is then row-normalized such that each row sums to 1. W is the sum of all ω_{ij} elements. x_i and x_j are either the initial coordinates of cell i or j (Supplementary Fig. 12c), the (vector) velocities of cell i or j at a given time-point (Fig. 6h) or the overall motility (displacement/time-tracked) of cell i or j (Supplementary Fig. 12e). \bar{x} is either the mean velocity at a given time-point or the mean motility. To generate a control sample, the Geary coefficient was also computed for cells with corresponding cell velocities or motilities randomized. The randomization process was repeated 100 times, and the 95% confidence interval of the random control group was presented.

Reporting Summary. Further information on research design is available in the Nature Research Reporting Summary linked to this article.

Data availability

The data that support the plots within this paper and other findings of this study are available from the corresponding author upon reasonable request.

References

- Wong, Y. J. et al. Revisiting the Stober method: inhomogeneity in silica shells. *J. Am. Chem. Soc.* **133**, 11422–11425 (2011).
- Palik, E. Optical parameters for the materials in HOC I and HOC II. In *Handbook of Optical Constants of Solids Vols 1–5*, 313–335 (Elsevier, 1997).

In the format provided by the authors and unedited.

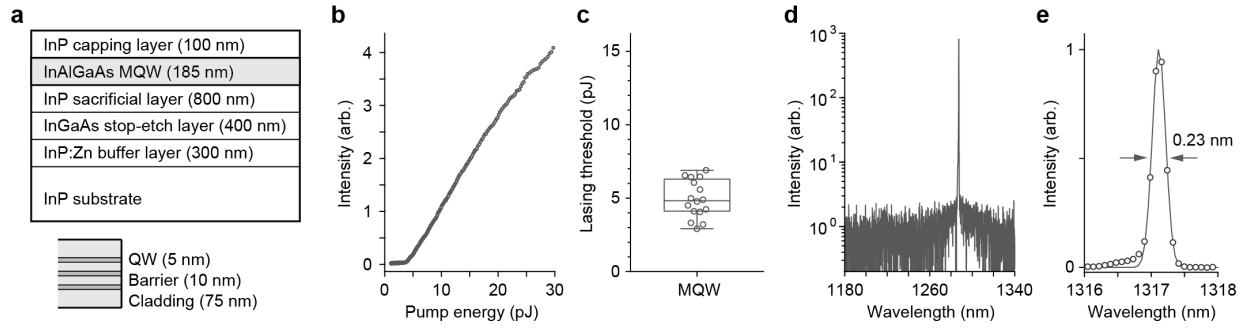
Wavelength-encoded laser particles for massively multiplexed cell tagging

Nicola Martino ^{1,2,7}, Sheldon J. J. Kwok^{1,2,3,7}, Andreas C. Liapis ^{1,2}, Sarah Forward², Hoon Jang⁴, Hwi-Min Kim⁴, Sarah J. Wu⁵, Jiamin Wu ^{2,6}, Paul H. Dannenberg^{1,2,3}, Sun-Joo Jang^{1,2}, Yong-Hee Lee⁴ and Seok-Hyun Yun ^{1,2,3*}

¹Harvard Medical School, Boston, MA, USA. ²Wellman Center for Photomedicine, Massachusetts General Hospital, Boston, MA, USA. ³Harvard-MIT Health Sciences and Technology, Massachusetts Institute of Technology, Cambridge, MA, USA. ⁴Department of Physics, Korea Advanced Institute of Science and Technology, Daejeon, South Korea. ⁵Department of Mechanical Engineering, Massachusetts Institute of Technology, Cambridge, MA, USA. ⁶Department of Automation, Tsinghua University, Beijing, China. ⁷These authors contributed equally: Nicola Martino and Sheldon J. J. Kwok.

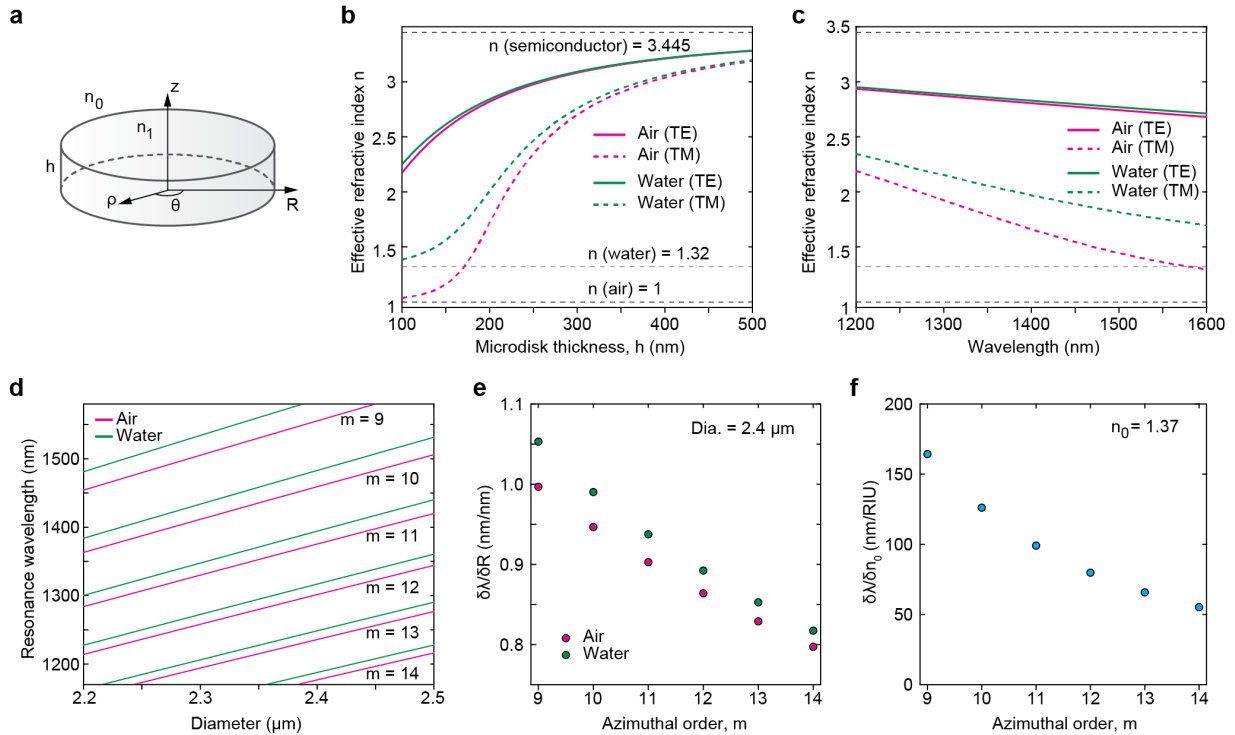
*e-mail: syun@hms.harvard.edu

Supplementary Figure 1



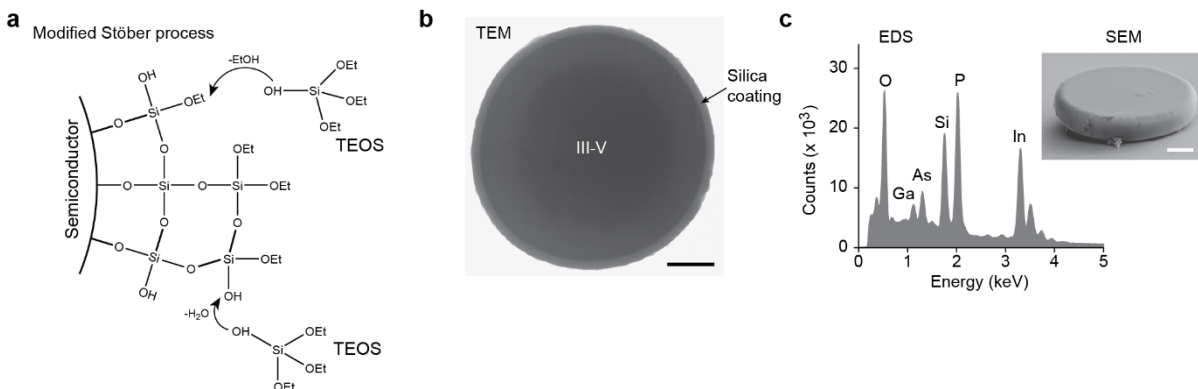
Optical characterization of MQW-based microdisks. **a**, Schematic diagram of the epitaxial wafer used for fabrication of MQW microdisks. **b**, Typical threshold curve (output intensity vs pump energy) of a MQW microdisk measured in air suspended on pillar. **c**, Distribution of threshold energy for MQW microdisks lasers ($N = 16$). **d**, Semi-logarithmic plot of a typical laser output spectrum of a typical MQW microdisk laser above lasing threshold. **e**, Gaussian fit of the linewidth of a MQW laser emission with a FWHM of 0.23 nm.

Supplementary Figure 2



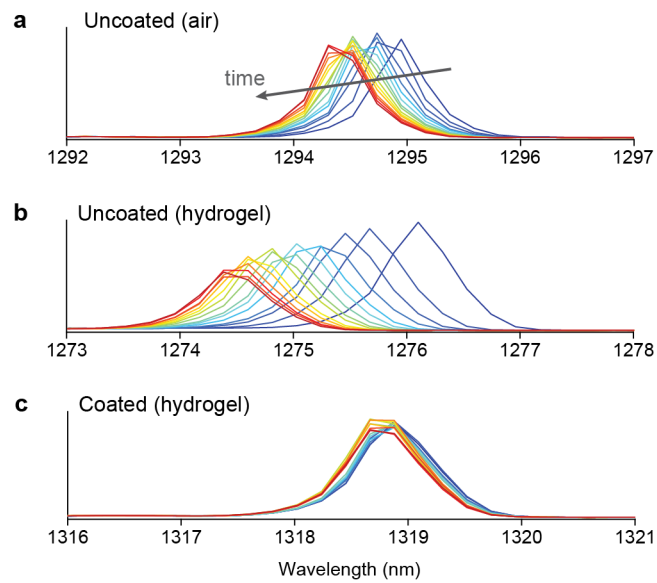
Theoretical calculation and simulations of microdisk resonances. **a**, Schematic of the microdisk geometry; n_0 and n_1 are the refractive indexes of the environment and semiconductor respectively, and R and h are the microdisk radius and thickness respectively. **b-c** Effective refractive index of a microdisk as a function of thickness (b) and of wavelength (c). The calculations were performed in air ($n_0 = n_{\text{air}} = 1$) and in water ($n_0 = 1.32$) for both the TE and TM modes. The refractive index of the semiconductor was set at $n_1 = 3.445$. As the resonator thickness gets smaller, the value of n_{eff} for the TM modes drops much faster than that for the TE ones. **d**, Resonance wavelengths of the TE modes for a semiconductor-only microdisk cavity ($h = 200$ nm) with a diameter varying from 2.2 to 2.5 μm , both in air and water, in the relevant spectral region for this work. **e**, Sensitivity of the resonance wavelength to changes in the microdisk radius, both in air and water, calculated for small variations around a design radius of $R = 1.2 \mu\text{m}$ ($h = 200$ nm). **f**, Sensitivity of the resonance wavelength to changes in the external refractive index, calculated for small variations around the typical value in the cytoplasm $n_0 = 1.37$ ($R = 1.2 \mu\text{m}$, $h = 200$ nm).

Supplementary Figure 3



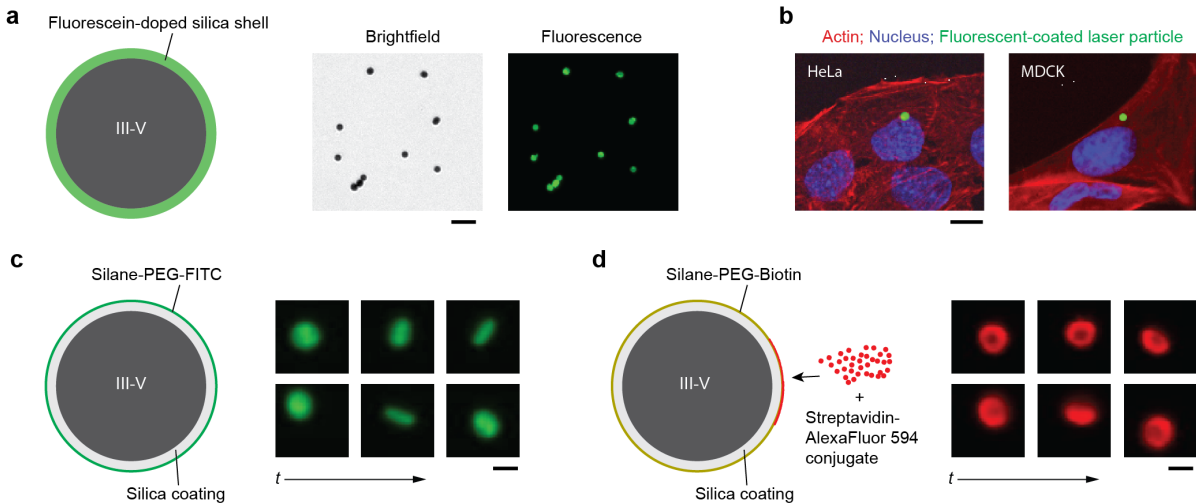
Silica coating of semiconductor microdisks. **a**, Schematic of the modified Stober process for silica coating. **b**, TEM image of a coated microdisk showing the thickness and uniformity of the silica layer. Scale bar: 500 nm. **c**, EDS elemental analysis of a coated microdisk (SEM in inset, scale bar: 500 nm), demonstrating the presence of the silica shell (Si, O) around the III-V semiconductor core (In, Ga, As, P).

Supplementary Figure 4



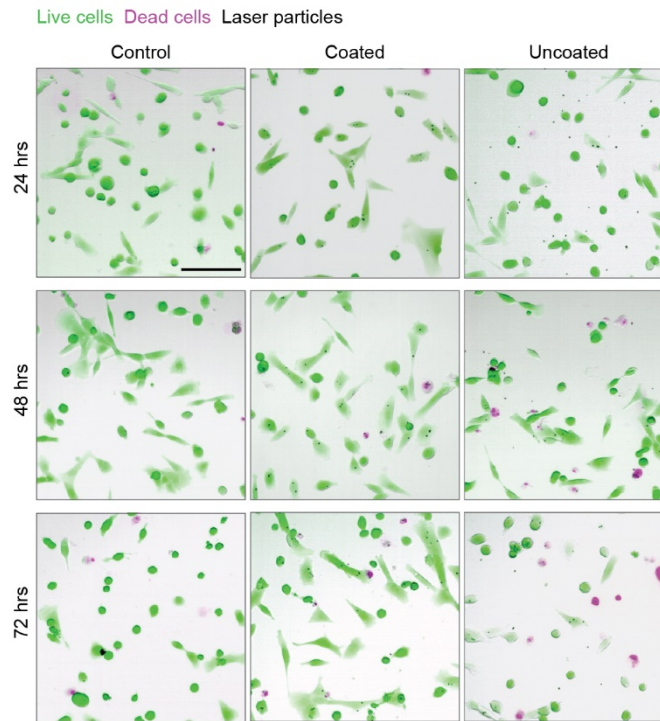
Stability of laser particles under continuous illumination. Representative spectra of microdisk emission during the degradation experiment of Fig. 4b, c for an uncoated microdisk in air (**a**), uncoated microdisk in hydrogel (**b**) and coated microdisk in hydrogel (**c**). The spectra are color coded based on time passed since the beginning of the experiment.

Supplementary Figure 5



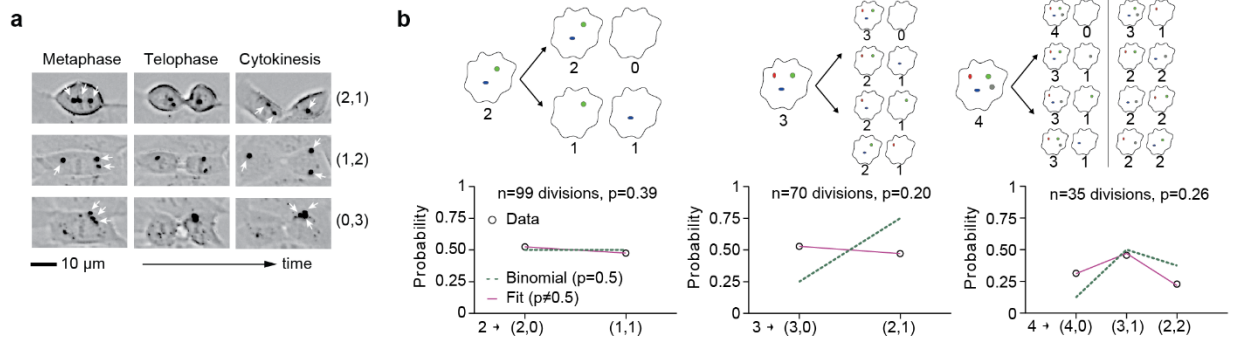
Functionalization of silica-coated laser particles. **a**, Fluorescent LPs were fabricated by doping the silica shell with fluorescein dyes (see Methods). Brightfield and fluorescence images of LPs showing green fluorescence from the fluorescein-doped silica shell. **b**, Fluorescence image of cells containing green-fluorescent LPs. Fixed HeLa and MDCK-II cells were stained with Alexa Fluor 594 Phalloidin (actin: red), and DAPI (nucleus: blue). Scale bar, 10 μm . **c-d**, Functionalization of silica coated LPs with poly(ethylene glycol)-fluorescein (PEG-FITC) or PEG-biotin. To confirm biotinylation, a red fluorescent streptavidin conjugate was added (d). Fluorescence images confirm encapsulation of the LPs with PEG (green, c), and biotin (red, d). Fluorescence time-lapse images show LPs undergoing Brownian motion in aqueous solution. Scale bar, 2 μm .

Supplementary Figure 6



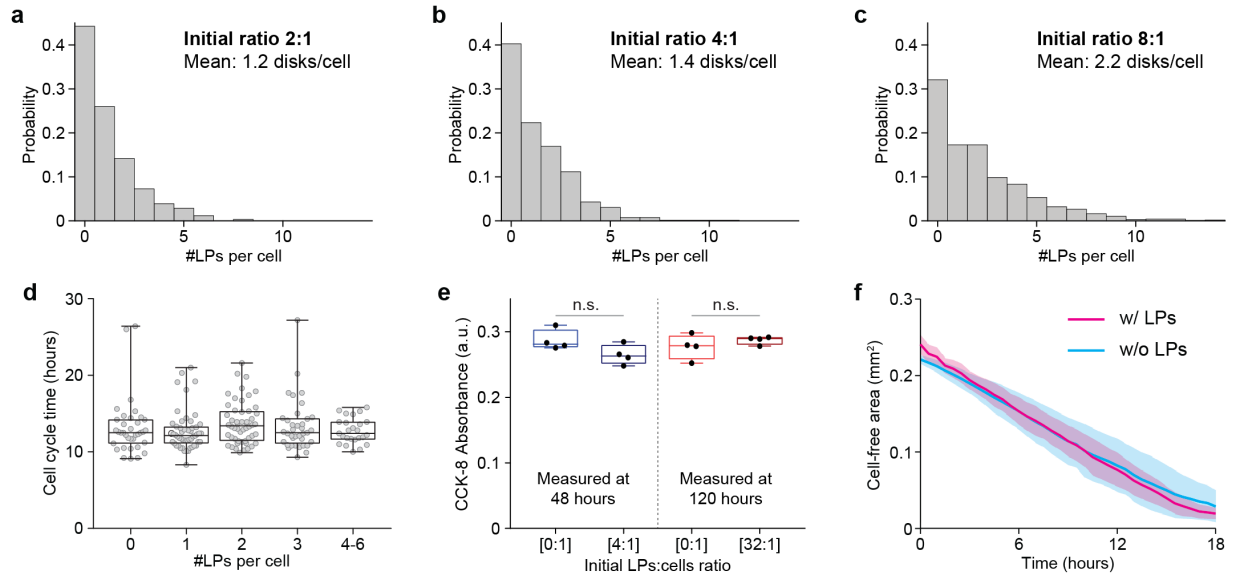
Live/dead imaging of cells with intracellular laser particles. Live/dead fluorescence staining of MDCK-II cells after incubation with coated, uncoated and no LPs (control) for 24, 48 and 72 h. Live cells and dead cells are labelled green (calcein-AM) and red (ethidium homodimer-1), respectively. Quantification of this data ($N = 12$ images per condition, about 100 cells per image) is shown in Fig. 4f. Scale bar: 100 μm .

Supplementary Figure 7



Mitotic partitioning of laser particles. **a**, Brightfield time-lapse images of MDCK-II cells showing mitotic partitioning of internalized LPs. Three examples are shown, where three particles (arrows) inside a single mother cell are transferred to two daughter cells at different ratios, 2:1 (1:2) or 0:3. Scale bar: 10 μ m. **b**, Analysis of intracellular LPs segregation with cell division. Cell division events of MDCK-II cells containing 2, 3 or 4 LPs were annotated. The data (open black circles) shows the probability of different cell division events (e.g. $3 \rightarrow (2,1)$ indicates that the parent cell contains 3 LPs, and the daughter cells receive 2 and 1 respectively). The dotted green line shows the expected binomial probabilities assuming the probability of transmission to either daughter cell is equal ($p = 0.5$). The magenta line shows fitting of the experimental data to an asymmetric binomial distribution.

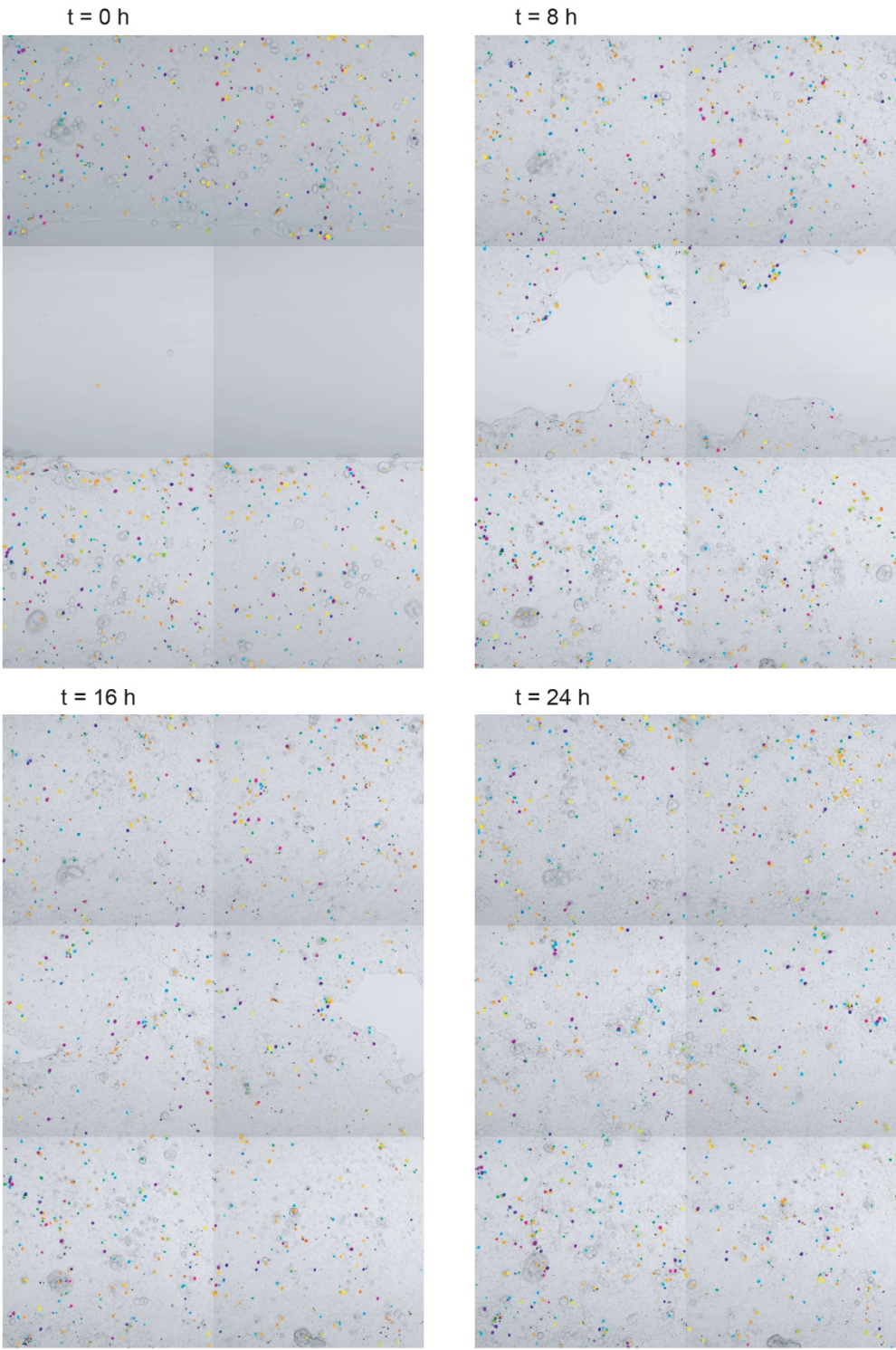
Supplementary Figure 8

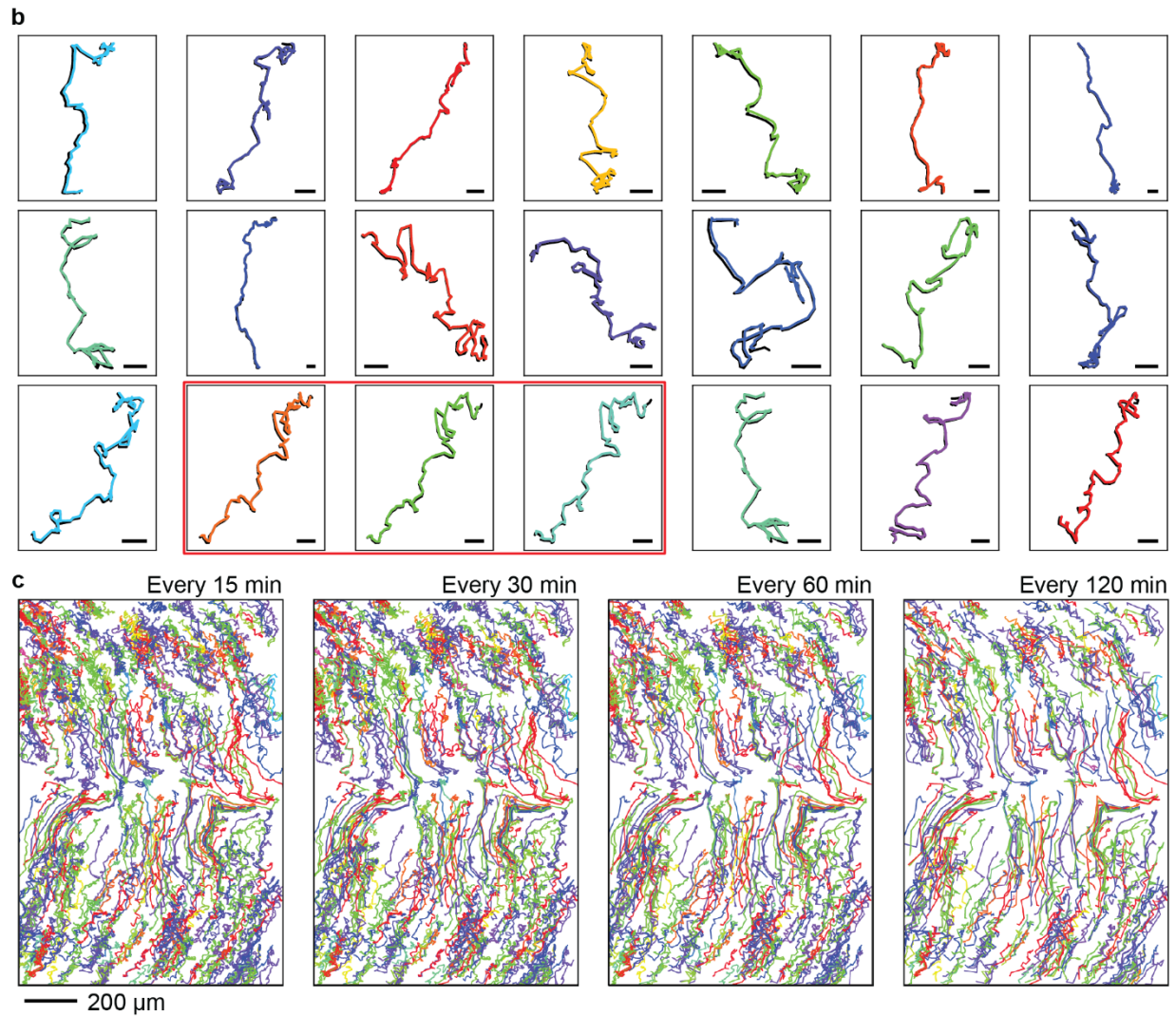


Laser particles uptake and biocompatibility assays. Histogram of the number of LPs internalized by MDCK-II cells after 24 hours incubation with LPs at initial LPs-to-cells concentrations of (a) 2:1 ($N = 592$ cells), (b) 4:1 ($N = 815$ cells) and 8:1 ($N = 1054$ cells). d, Cell cycle time measured for 201 cells carrying different numbers of LPs using time-lapse imaging. A one-way ANOVA [$F(4,197) = 1.021$] for the effect of particle number was not significant ($p > 0.05$). e, Effect of LPs on cellular proliferation measured by the CCK-8 assay. MDCK-II cells were incubated with 4:1 particle:cell ratio (measured at 48 h), and incubated with 32:1 ratio (measured at 120 h), compared to controls (no LPs). A two-tailed, unpaired t-test revealed no significant difference in proliferation rate between cells with and without LPs ($p > 0.05$, $N = 4$ for each condition). f, Measured size of gap in a wound-healing assay conducted using MDCK-II cells cultured with (magenta; initial concentration 4:1) and without (cyan) LPs. The gap closure (wound healing) time is unaffected by the LPs.

Supplementary Figure 9

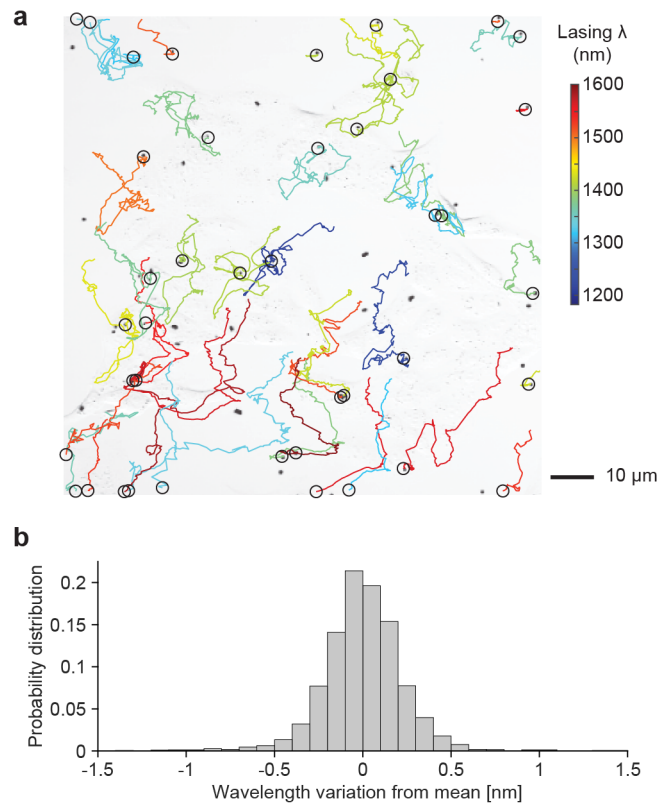
a





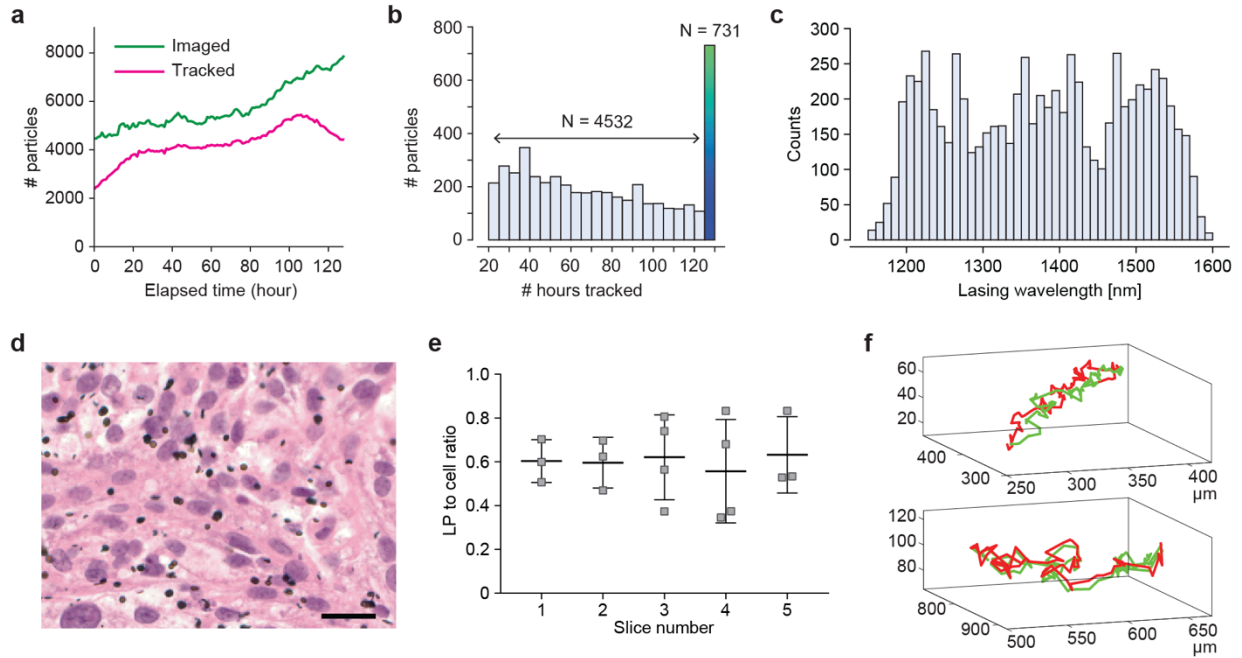
Validation of tracking algorithm. **a**, Overlay of brightfield and LASE imaging at different time points during a wound-healing assay of LP-tagged MDCK-II cells. **b**, Comparison between the paths of $N = 21$ LPs manually tracked from the brightfield image (black lines) with the corresponding traces obtained by the analysis of the LASE data (colored lines). The three LPs in the red box are in the same cell; the tracking algorithm is able to correctly follow them despite their paths intersect because of they are spectrally distinguished. All scale bars are 20 μm . **c**, Paths of all the LPs tracked for more than 20 h by our algorithm applied to sub-sampled datasets at increasing time intervals (15, 30, 60 and 120 minutes).

Supplementary Figure 10



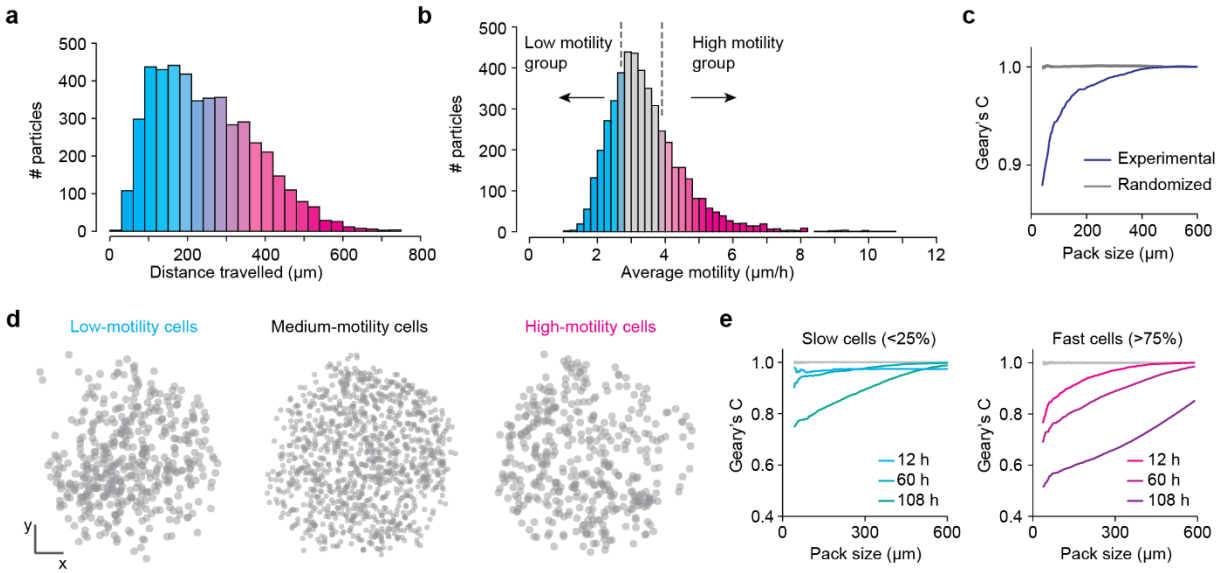
Wavelength variation of intracellular laser particles. a, Time-lapse wavelength-position traces of individual LPs superimposed with a brightfield transmission image of the MDCK cell culture. Measurements were taken every 10 min over a duration of 33 h. Circles indicate the initial positions of LPs, and the color of each traces represents lasing wavelength. **b**, Distribution of the variations in the measured wavelength at each time point from the mean value during the 33 hours tracking. Only data for LPs that were inside cells for the entire duration of the experiment are reported.

Supplementary Figure 11



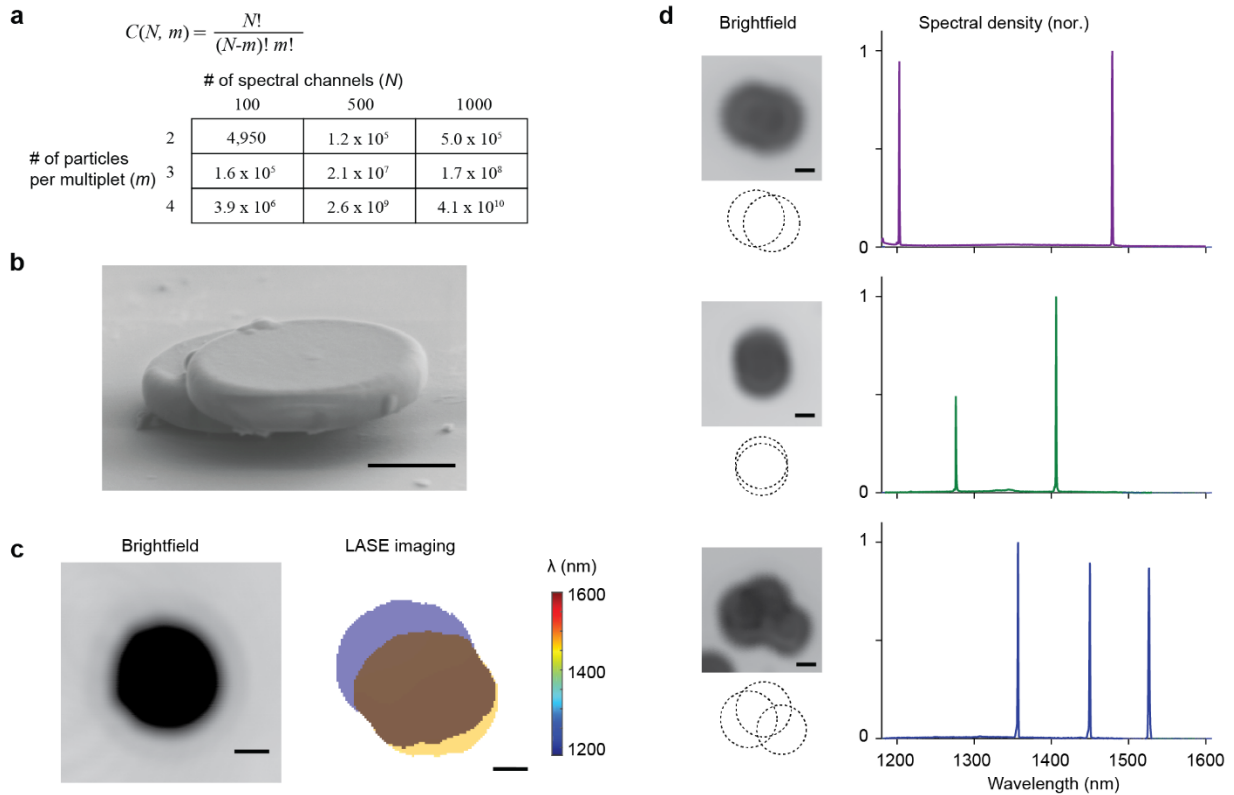
Imaging laser particles in a tumor spheroid. **a**, Number of LPs imaged at each time point during the time-lapse imaging of the tumor spheroid, compared to the ones that are tracked (only particles that were tracked for more than 24 hours are considered). **b**, Histogram of tracking time for all tracked LPs. **c**, Wavelength distribution of the LPs tracked in the experiment, uniformly covering the entire 1180-1580 nm spectral range as described in Fig. 2. **d**, H&E-stained section of the tumor spheroid fixed and imaged after the tracking experiment (scale bar: 20 μm). **e**, Statistics of the LP-to-cell ratio in 5 slices taken from different locations in the tumor spheroid. Squares: raw data obtained from 3 to 4 images per slice. **f**, Examples of two LPs (green and red) following the same paths throughout their entire tracking duration. Such particles are considered to have been in the same cell.

Supplementary Figure 12



Motility analysis of LP-tagged cells. **a**, Statistics of the traveled distance for each cell during the tracking time, calculated as the (scalar) sum of the displacements at each time interval. **b**, Statistics of average motility for each tracked cell, calculated as total travel distance divided by tracking time. The low- and high-motility cells were determined as the bottom and top quartile of the histogram, respectively, and the remaining cells are classified as medium motility. **c**, Geary's coefficient computed for spatial autocorrelation of overall motility to initial cellular coordinates, presented as a function of cellular pack size. The randomized control is computed by random assignment of motilities to cells, and the 95% confidence interval of 100 simulations is shown. The difference between experimental and randomized data indicates strong spatial autocorrelation below approximately 200 μm . **d**, Position at early times ($t = 12$ h) of low, medium and high motility cells within the spheroid. Scale bars, 100 μm . **e**, Geary's coefficient computed for spatial autocorrelation of instantaneous velocities to cellular position at given times. Slow and fast cells represent the bottom and top quartiles of instantaneous velocities at each time, respectively. Randomized control (95% confidence interval of 100 simulations) is shown for each group. The data indicates significantly higher spatial autocorrelation for fast cells before (12 h), at the onset (60 h) and during (108 h) invasion.

Supplementary Figure 13



Multiplet microdisk laser particles. **a**, Theoretical number of uniquely identifiable spectra or optical barcodes when multiple laser particles are combined to form a multiplet. The number of unique combinations is given for the # of particles per multiplet (m) and the number of distinguishable spectral channels (N). **b**, SEM image of a multiplet that was formed after three cycles of silica coating. Multiple cycles of Stöber coating results in occasional formation of laser particle aggregates. The silica coating thickness is approximately 150 nm. Scale bar: 1 μm . **c**, Brightfield and LASE image of a laser particle doublet. Lasing peaks were observed at 1197 nm, 1491 nm or both, depending on the spatial overlap of each disk in the multiplet and the pump beam. Scale bars: 1 μm . **d**, Brightfield images and emission spectra of doublet and triplet particles formed during multiple coating cycles. Scale bars: 1 μm .

Supplementary Videos

Supplementary Video 1: Macropinocytosis of microdisk laser particles

This video shows uptake of microdisk laser particles by MDCK-II cells.

Supplementary Video 2: Time-lapse brightfield imaging of intracellular laser particles

This video shows laser particle uptake by MDCK-II cells, and their migration and proliferation behaviors over several days of imaging at 5 min intervals.

Supplementary Video 3: Time-lapse brightfield imaging of intracellular laser particles

This video shows laser particle uptake by MDCK-II cells, and their migration and proliferation behaviors over several days of imaging at 5 min intervals. One particular cell in the upper part of the video is shown to uptake more than 10 particles and subsequently undergoes apoptosis.

Supplementary Video 4: Time-lapse brightfield imaging of intracellular laser particles

This video shows the uptake of one laser particle by a MDCK-II cell. At approximately $t = 2.5$ h, the laser particle appears to leave the cell momentarily. However, prior to $t = 3$ h, the laser particle may not be completely internalized and appears to be resting within the lamellipodium or cell surface. Following $t = 3$ h, the laser particle is completely internalized, and the cell successfully divides ($t = 13$ h), passing the particle to one of its daughter cells. We were not able to identify any clear evidence of exocytosis in our imaging data.

Supplementary Video 5: Time-lapse imaging of spheroid evolution

This video shows the time-lapse brightfield imaging collected during the 4T1 spheroid invasion assay (one frame every hour for 128 hours). The spheroid is observed growing in size at early times (up to 40 hours), and then cells start to invade the surrounding matrix.

Supplementary Video 6: Time-lapse imaging of cell movement in spheroid invasion assay

This video shows the instantaneous velocities of the tracked cells at each time point during the time-lapse imaging of the spheroid invasion assay. Each arrow represents the (vector) velocity of a single laser particle, color coded by its magnitude.

Supplementary Notes

Supplementary Note 1: WGM resonance modeling

Resonance wavelengths for bare microdisk resonators of different diameters were calculated using the effective index method¹ for a cylindrical resonator of radius R , thickness h and refractive index n_1 in an environment with refractive index n_0 (Supplementary Fig. 2a). The original 3-dimensional problem can be approximated to a 2D disk of effective refractive index $n_{eff}(\lambda)$, given for TE and TM modes by the solution of the implicit equations:

$$TE: \tan\left(\frac{\pi h}{\lambda} \sqrt{n_1^2 - n_{eff}^2}\right) = \sqrt{\frac{n_{eff}^2 - n_0^2}{n_1^2 - n_{eff}^2}} \quad (S1)$$

$$TM: \tan\left(\frac{\pi h}{\lambda} \sqrt{n_1^2 - n_{eff}^2}\right) = \frac{n_1^2}{n_0^2} \sqrt{\frac{n_{eff}^2 - n_0^2}{n_1^2 - n_{eff}^2}} \quad (S2)$$

These equations may have more than one solutions corresponding to different thickness modes of the disk. The maximum thickness h_{sm} , below which only the fundamental thickness mode is supported, is given by:

$$h_{sm} = \frac{\lambda}{2\sqrt{n_1^2 - n_0^2}} \quad (S3)$$

For a design wavelength of $\lambda = 1350$ nm and $n_1 = 3.445$, we obtain $h_{sm} = 205$ nm in air ($n_0 = 1$) and $h_{sm} = 212$ nm in water ($n_0 = 1.32$). The actual thickness of 200 nm satisfies the single-mode condition, $h < h_{sm}$.

We calculated the effective refractive indices of only the lowest-order TE and TM modes, as shown in Supplementary Fig. 2b, c. The TE modes have considerably higher n_{eff} than the TM modes, especially for thicknesses below h_{sm} . We thus focused our analysis on the TE modes, which are better confined and have higher Q-factors². The electromagnetic field profile of the TE modes for the 2D disk is given, in cylindrical coordinates, by¹:

$$H_z = \begin{cases} AJ_m(k_0 n_{eff} \rho) e^{-i(m\phi - \omega t)}, & \rho \leq R \\ BH_m^{(2)}(k_0 n_0 \rho) e^{-i(m\phi - \omega t)}, & \rho > R \end{cases} \quad (S4)$$

$$E_\rho = \frac{j\mu_0\omega}{k_0^2 n^2 \rho} \frac{\partial H_z}{\partial \rho}, \quad E_\phi = -\frac{j\mu_0\omega}{k_0^2 n^2} \frac{\partial H_z}{\partial \rho}, \quad E_z = H_\rho = H_\phi = 0$$

where J_l is the Bessel function of the first kind, $H_l^{(2)}$ is the Hankel function of the second kind, μ_0 is the vacuum permeability, m is the azimuthal order of the mode, A and B are normalization constant, ω and k_0 are the frequency and wavenumber. By applying the boundary conditions at the disk edge, i.e. the continuity of E_φ and H_z , we can derive the following relationship:

$$\frac{J_{m-1}(U) - J_{m+1}(U)}{UJ_m(U)} = \frac{H_{m-1}^{(2)}(Q) - H_{m+1}^{(2)}(Q)}{QH_m^{(2)}(Q)} \quad (S5)$$

where we have defined $U = k_0 n_{eff} R$ and $Q = k_0 n_0 R$. As both Eq. (S1) and Eq. (S4) depend only on n_{eff} and λ , they can be solved together to find the resonance wavelengths $\lambda_{m,p}$, where p is the radial order of the modes. The solutions for the resonance modes of microdisks with varying diameters are reported in Supplementary Fig. 2d, for both air and water as the external medium.

This model allows us to estimate how much the resonance wavelengths of the cavities are affected by changes in the various parameters of the problem. For microdisks of 2 μm in diameter (Fig. 1c), the sensitivity to small variations in microdisk radius is $\delta\lambda/\delta R = 1.07$ and 1.01 nm/nm respectively for $m = 9$ and 10. For diameters in the 2.2 – 2.5 μm range (Fig. 2) the $\delta\lambda/\delta R$ ranges from 0.8 to 1.05 nm/nm as shown in Supplementary Fig. 2e.

The sensitivity of the resonance wavelength to small variations in external refractive index ($\delta\lambda/\delta n_0$) at a design radius of 1.2 μm is shown in Supplementary Fig. 2f. $\delta\lambda/\delta n_0$ varies from 160 nm/RIU for $m = 9$ to 50 nm/RIU for $m = 14$.

Supplementary Note 2: Detection and tracking algorithm validation

The algorithm used for detecting and tracking LPs (described in the Methods section) was validated on an in-vitro time-lapse imaging dataset of a wound-healing assay. Brightfield and LASE images were acquired simultaneously every 15 minutes for 28 hours (Supplementary Fig. 9). From the brightfield image taken at 0 h we observed 899 microdisks (dark spots), while the LASE microscopy algorithm detected 757 LPs. This discrepancy is primarily because we used a fixed pump power at a modified level to avoid any thermal degradation, and some (~142) of the LPs did not reach lasing threshold at the pump power. This false-negative error is not critical as we don't intend to track every single cell (particle). This rate can be reduced by making LPs with more uniform quality in terms of lasing threshold. The algorithm described in the manuscript was applied to obtain cellular trajectories. Supplementary Fig. 9 shows the paths of the $N = 730$ LPs,

all of which were tracked for longer than 20 h. To check if the algorithm correctly computes the paths of the LPs, we randomly selected 21 laser particles in the brightfield images and manually followed them (occasionally using the wavelength emission information to help tracking). These trajectories served as ground truth data. For all 21 cases, we found a very good match between the ground truth data and the LPs paths extracted by our tracking algorithm. This result is illustrated in Supplementary Fig. 9. We found that 3 out of the 21 LPs had almost identical trajectories, which we interpreted that they were in the same cells (paths in the red box in Supplementary Fig. 9). The LASE tracking algorithm correctly follows their trajectories even when their paths crossed each other.

To evaluate the adequacy of the 1-hour interval we used in the tumor spheroid tracking experiment described in the main text, we applied the spectral-spatial algorithm to the same dataset described above sub-sampled every 30, 60 and 120 minutes, respectively. Of the 730 microdisks tracked from the full LASE microscopy dataset, this number reduced to 715 microdisks with 30 min interval, 696 microdisks with 60 min interval, and 660 with 120 min interval (Supplementary Fig. 9). With the 60 min interval, about 5% of LPs are lost during tracking. Although undesirable, this drop-out case is not critical when tracking every cell is not necessary and should be acceptable for most experiments.

Supplementary Note 3: Errors in laser particle identification

Consider a series of laser particles (i 's) with incrementally increasing nominal wavelengths $\lambda_{0,i}$ with an interval of Δ . We assume that spectral measurement has a Gaussian distribution with a standard deviation σ . When $\Delta \gg \sigma$, the series of particles can be correctly identified by ranking the measured wavelengths in increasing order. However, a finite probability for error exists when the measured rank order between two adjacent particles is reversed due to the measurement uncertainty. The probability that a single measurement of the i -th particle will yield a value λ_i is described by a probability density function P_i :

$$pdf_i(\lambda_i) = \frac{1}{\sqrt{2\pi}\sigma} e^{-\left(\frac{\lambda_i - \lambda_{0,i}}{\sqrt{2}\sigma}\right)^2} \quad (S6)$$

For correct identification, the measured wavelength λ_i the i -th particle should fall between the measured values of the $(i-1)$ -th and $(i+1)$ -th particles, i.e. $\lambda_{i-1} < \lambda_i < \lambda_{i+1}$. When $\Delta \lambda \gg \sigma$, the

dominant error is due to nearest neighbor swapping, which occurs when $\lambda_i < \lambda_{i-1}$ or $\lambda_i < \lambda_{i+1}$. The probability of this mismatching error is given:

$$E(\lambda_i) = P[\lambda_i < \lambda_{i-1}] + P[\lambda_i > \lambda_{i+1}] \quad (S7)$$

The total error probability P_{err} of incorrectly assigning the i -th particle is expressed as:

$$P_{err} = \int_{-\infty}^{+\infty} pdf_i(\lambda_i)E(\lambda_i)d\lambda_i = \int_{-\infty}^{+\infty} pdf_i(\lambda_i) \left[\int_{\lambda_i}^{+\infty} pdf_{i-1}(\lambda)d\lambda + \int_{-\infty}^{\lambda_i} pdf_{i+1}(\lambda)d\lambda \right] d\lambda_i \quad (S8)$$

Using (S6), we find:

$$P_{err} = 1 - erf\left(\frac{\Delta}{2\sigma}\right) \quad (S9)$$

where erf is the error function. For $\Delta = 1$ nm and $\sigma = 0.18$ nm, we obtain $P_{err} = 8.6 \times 10^{-5}$.

Another way of identifying laser particles is to assign fixed bins of a width equal to Δ around the nominal wavelengths $\lambda_{0,i}$ and match the measured value λ_i to a corresponding bin. The probability of error in this case is given by:

$$P_{err} = \int_{-\infty}^{\lambda_{0,i}-\Delta/2} pdf_i(\lambda)d\lambda + \int_{\lambda_{0,i}+\Delta/2}^{+\infty} pdf_i(\lambda)d\lambda \quad (S10)$$

Therefore, we find:

$$P_{err} = 1 - erf\left(\frac{\Delta}{2\sqrt{2}\sigma}\right) \quad (S11)$$

For $\Delta = 1$ nm and $\sigma = 0.18$ nm, we have in this case $P_{err} = 5.5 \times 10^{-3}$.

References

1. Andronico, A. *et al.* Semiconductor microcavities for enhanced nonlinear optics interactions. *J. Eur. Opt. Soc. Rapid Publ.* **3**, 08030 (2008).
2. Frateschi, N. C. & Levi, A. F. J. The spectrum of microdisk lasers. *J. Appl. Phys.* **80**, 644–653 (1996).

Reporting Summary

Nature Research wishes to improve the reproducibility of the work that we publish. This form provides structure for consistency and transparency in reporting. For further information on Nature Research policies, see [Authors & Referees](#) and the [Editorial Policy Checklist](#).

Statistical parameters

When statistical analyses are reported, confirm that the following items are present in the relevant location (e.g. figure legend, table legend, main text, or Methods section).

n/a Confirmed

- The exact sample size (n) for each experimental group/condition, given as a discrete number and unit of measurement
- An indication of whether measurements were taken from distinct samples or whether the same sample was measured repeatedly
- The statistical test(s) used AND whether they are one- or two-sided
Only common tests should be described solely by name; describe more complex techniques in the Methods section.
- A description of all covariates tested
- A description of any assumptions or corrections, such as tests of normality and adjustment for multiple comparisons
- A full description of the statistics including central tendency (e.g. means) or other basic estimates (e.g. regression coefficient) AND variation (e.g. standard deviation) or associated estimates of uncertainty (e.g. confidence intervals)
- For null hypothesis testing, the test statistic (e.g. F , t , r) with confidence intervals, effect sizes, degrees of freedom and P value noted
Give P values as exact values whenever suitable.
- For Bayesian analysis, information on the choice of priors and Markov chain Monte Carlo settings
- For hierarchical and complex designs, identification of the appropriate level for tests and full reporting of outcomes
- Estimates of effect sizes (e.g. Cohen's d , Pearson's r), indicating how they were calculated
- Clearly defined error bars
State explicitly what error bars represent (e.g. SD, SE, CI)

Our web collection on [statistics for biologists](#) may be useful.

Software and code

Policy information about [availability of computer code](#)

Data collection

Confocal images were taken using FluoVIEW software from Olympus; LASE imaging was performed with a custom-made Python software controlling acquisition from the NIR spectrometer

Data analysis

Data were analyzed using custom MATLAB scripts to extract lasing information from spectra (peak wavelength, power, thresholds), to cluster spatial data for localization of laser particles and to simulate WGM resonance

For manuscripts utilizing custom algorithms or software that are central to the research but not yet described in published literature, software must be made available to editors/reviewers upon request. We strongly encourage code deposition in a community repository (e.g. GitHub). See the Nature Research [guidelines for submitting code & software](#) for further information.

Data

Policy information about [availability of data](#)

All manuscripts must include a [data availability statement](#). This statement should provide the following information, where applicable:

- Accession codes, unique identifiers, or web links for publicly available datasets
- A list of figures that have associated raw data
- A description of any restrictions on data availability

The code for the analyses described in this paper is available from the corresponding author upon reasonable request.

Field-specific reporting

Please select the best fit for your research. If you are not sure, read the appropriate sections before making your selection.

Life sciences Behavioural & social sciences Ecological, evolutionary & environmental sciences

For a reference copy of the document with all sections, see [nature.com/authors/policies/ReportingSummary-flat.pdf](https://www.nature.com/authors/policies/ReportingSummary-flat.pdf)

Life sciences study design

All studies must disclose on these points even when the disclosure is negative.

Sample size	<input type="text" value="No specific sample size was chosen apriori"/>
Data exclusions	<input type="text" value="No data was excluded"/>
Replication	<input type="text" value="All data was reproducible"/>
Randomization	<input type="text" value="Not applicable"/>
Blinding	<input type="text" value="Not applicable"/>

Reporting for specific materials, systems and methods

Materials & experimental systems

n/a	Included in the study
<input checked="" type="checkbox"/>	<input type="checkbox"/> Unique biological materials
<input checked="" type="checkbox"/>	<input type="checkbox"/> Antibodies
<input type="checkbox"/>	<input checked="" type="checkbox"/> Eukaryotic cell lines
<input checked="" type="checkbox"/>	<input type="checkbox"/> Palaeontology
<input type="checkbox"/>	<input checked="" type="checkbox"/> Animals and other organisms
<input checked="" type="checkbox"/>	<input type="checkbox"/> Human research participants

Methods

n/a	Included in the study
<input checked="" type="checkbox"/>	<input type="checkbox"/> ChIP-seq
<input checked="" type="checkbox"/>	<input type="checkbox"/> Flow cytometry
<input checked="" type="checkbox"/>	<input type="checkbox"/> MRI-based neuroimaging

Eukaryotic cell lines

Policy information about [cell lines](#)

Cell line source(s)	<input type="text" value="HeLa (ATCC), 4T1 (ATCC), MDCK-II (ECACC), HEK-293 (gift from Prof. Adam E. Cohen, Harvard University)"/>
Authentication	<input type="text" value="Cell morphology was as expected, no other authentication procedures"/>
Mycoplasma contamination	<input type="text" value="Cell lines were not tested for mycoplasma"/>
Commonly misidentified lines (See ICLAC register)	<input type="text" value="None"/>

Animals and other organisms

Policy information about [studies involving animals](#); [ARRIVE guidelines](#) recommended for reporting animal research

Laboratory animals	<input type="text" value="Female mouse, mTmG-B6 (Jackson Laboratories), ~7 months"/>
Wild animals	<input type="text" value="None"/>
Field-collected samples	<input type="text" value="None"/>